THE JOURNAL OF PHYSICAL CHEMISTRY LETTERS
A JOURNAL OF THE AMERICAN CHEMICAL SOCIETY

pubs.acs.org/JPCL Letter

Femtosecond X-ray Spectroscopy Directly Quantifies Transient Excited-State Mixed Valency

Chelsea Liekhus-Schmaltz, Zachary W. Fox, Amity Andersen, Kasper S. Kjaer, Roberto Alonso-Mori, Elisa Biasin, Julia Carlstad, Matthieu Chollet, James D. Gaynor, James M. Glownia, Kiryong Hong, Thomas Kroll, Jae Hyuk Lee, Benjamin I. Poulter, Marco Reinhard, Dimosthenis Sokaras, Yu Zhang, Gilles Doumy, Anne Marie March, Stephen H. Southworth, Shaul Mukamel, Amy A. Cordones, Robert W. Schoenlein, Niranjan Govind,* and Munira Khalil*

Cite This: *J. Phys. Chem. Lett.* 2022, 13, 378−386 Read Online

ACCESS | Metrics & More | Article Recommendations | Supporting Information

ABSTRACT: Quantifying charge delocalization associated with short-lived photoexcited states of molecular complexes in solution remains experimentally challenging, requiring local element specific femtosecond experimental probes of time-evolving electron transfer. In this study, we quantify the evolving valence hole charge distribution in the photoexcited charge transfer state of a prototypical mixed valence bimetallic iron−ruthenium complex, $[(CN)_5Fe^{II}CNRu^{III}(NH_3)_5]^-$, in water by combining femtosecond X-ray spectroscopy measurements with time-dependent density functional theory calculations of the excited-state dynamics. We estimate the valence hole charge that accumulated at the Fe atom to be 0.6 ± 0.2, resulting from excited-state metal-to-metal charge transfer, on an ∼60 fs time scale. Our combined experimental and computational approach provides a spectroscopic ruler for quantifying excited-state valency in solvated complexes.

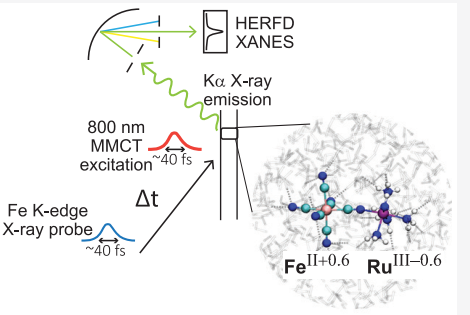

The field of inorganic mixed valency has contributed significantly to our fundamental understanding of intramolecular electron transfer since the synthesis of the Creutz-Taube ion reported in 1969.[1] One of the questions in the field of mixed valency that continues to garner much experimental and theoretical interest is the precise determination of the extent of electron delocalization.[2,3] Electron delocalization has largely been studied under the Robin−Day classification system, which attributes the extent of delocalization to electronic coupling between two metal centers: class I (uncoupled, localized charges), class II (moderately coupled), and class III (strongly coupled, delocalized charges).[4] The Robin−Day classification is based on infrared (IR) and near IR spectroscopy, which are indirect probes of the valence charge distribution, making quantitative determinations of electron delocalization between the transition metal centers a challenging problem. The challenge is compounded when trying to determine mixed valency associated with short-lived excited electronic states. The lack of direct experimental measurements of ultrafast time-evolving electronic character makes quantitative connection to theory difficult, resulting in a significant knowledge gap for developing predictive design principles to harness molecular mixed valency for molecular energy capture or electron transfer in chromophore−catalyst assemblies.

Time-resolved optical, IR, and two-dimensional (2D) spectroscopies have made important measurements of ultrafast charge transfer in transition metal mixed valence systems by measuring relevant solvent-dependent kinetic parameters of electron transfer and identifying the role of the coupled high-frequency cyanide vibrations in the photoinduced forward and back electron transfer processes.[5−13] However, ultrafast optical and IR studies are inherently limited in their ability to map electronic dynamics at high spatial resolution, making it challenging to determine the extent of ultrafast excited-state mixed valency in molecular systems. In contrast to ultrafast optical and IR studies, time-resolved X-ray absorption and X-ray emission spectroscopies (XAS and XES, respectively) probe transitions involving core level atomic orbitals, making them selective and sensitive to local atomic and electronic changes.[14−20] Recent advances in X-ray free electron lasers (XFELs), such as the Linac Coherent Light Source (LCLS), enable the production of high-intensity, tunable, <45 fs X-ray pulses for ultrafast XES and XAS measurements of atomic and electronic structural dynamics of dilute solution samples.[21,22] These time-resolved X-ray studies have successfully monitored

Received: November 3, 2021
Accepted: December 28, 2021
Published: January 5, 2022

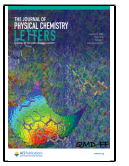

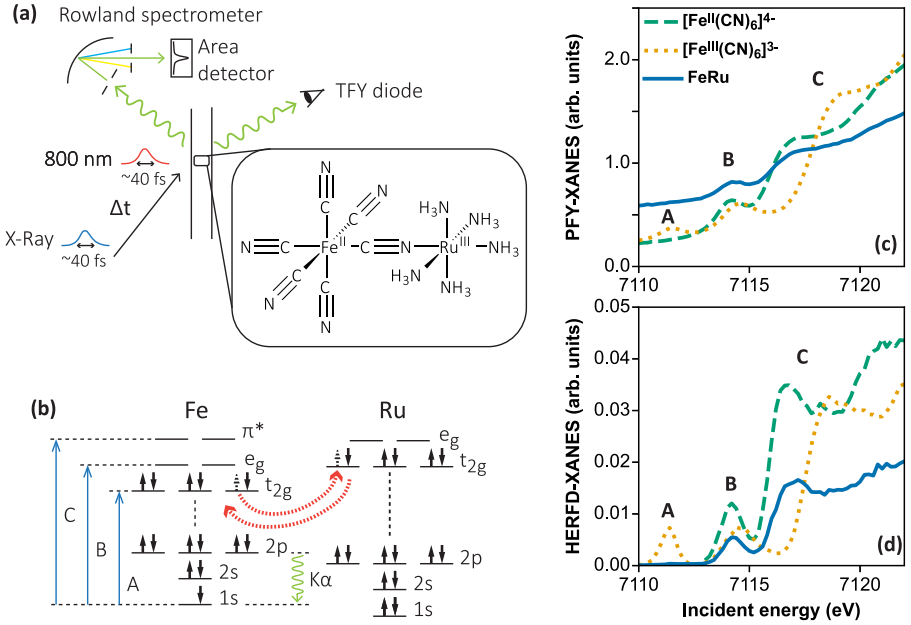

Figure 1. (a) Experimental configuration at the XPP endstation at LCLS for performing transient HERFD-XANES. The sample, 30 mM FeRu (shown in the inset) dissolved in water, is delivered via a 50 μm circular liquid jet in a He-filled chamber. The MMCT transition is excited using an ~40 fs full width at half-maximum (fwhm), 800 nm, pulse and probed with an ~40 fs fwhm long X-ray pulse whose incident energy is scanned from 7110 to 7120 eV using an upstream monochromator (not shown). (b) Relevant atomic and molecular orbitals in FeRu. The MMCT excitation and resulting BET are shown as the red dashed line, and the core level transitions probed by the X-ray probe are shown as blue arrows. The HERFD-XANES probe is scanned over the 1s to t_{2g}, e_g, and π^* transitions, and the peaks are labeled as A, B, and C, respectively. The time-resolved HERFD-XANES fluorescence signal is measured at the peak of the Kα_1 ($2p_{3/2} \rightarrow 1s$) transition by the Rowland spectrometer, shown by the green line. The ground-state XANES [in partial fluorescence yield (PFY) mode] and HERFD-XANES spectra of FeRu (30 mM) and two model complexes, $K_4Fe^{II}(CN)_6$ (100 mM) and $K_3Fe^{III}(CN)_6$ (100 mM), in aqueous solutions, at the Fe K-edge are shown in panels c and d, respectively. For all three complexes, the B ($1s \rightarrow 3de_g$) and C ($1s \rightarrow \pi^*$) peaks are visible, while the A ($1s \rightarrow 3dt_{2g}$) peak appears only in the spectra of $K_3Fe^{III}(CN)_6$ because of a t_{2g} vacancy. Comparing the XANES measurement taken in the PFY mode and the HERFD-XANES spectra shows how HERFD-XANES spectroscopy significantly reduces the background. The PFY-XANES spectra are obtained by summing over the emission frequencies of the resonant inelastic X-ray scattering (RIXS) spectral maps. See Figure S5 for further details.

excited-state dynamics such as spin crossovers, nuclear oscillations, and electron transfer in solvated transition metal complexes.[23−33]

Obtaining quantitative microscopic information from ultrafast X-ray experiments requires accompanying simulations of the transient signals on electronic excited states. In the case of the mixed valence complexes, it is crucial to include explicit solute−solvent interactions to correctly model the electronic excited-state dynamics.[34] Currently, the state-of-the-art theoretical techniques for tackling transition metal complexes are based on wave function approaches.[35] However, these methods become computationally prohibitive for large solvated systems lacking high symmetry. In previous work, we have shown that ground-state quantum mechanics/molecular mechanics (QM/MM) dynamics at the density functional theory (DFT) level and excited-state computations with linear-response time-dependent density functional theory (LR-TDDFT) are sufficiently accurate to capture the ground-state and excited-state characteristics of these large, solvated transition metal complexes.[34,36,37] This has allowed us to analyze how the local solvation environment and explicit solute−solvent interactions influence the intensity and line shape of specific spectroscopic features from the infrared to X-ray wavelengths.[36]

In this Letter, we present a combined experimental and computational study to quantify the extent of ultrafast electron delocalization on the short-lived metal-to-metal charge transfer (MMCT) state of the mixed valence complex, $[(CN)_5Fe^{II}CNRu^{III}(NH_3)_5]^-$, FeRu for brevity, using femtosecond XAS at the Fe K-edge.[3,32−34] We use a high-resolution XAS technique, high-energy resolution fluorescence X-ray absorption near edge spectroscopy (HERFD-XANES). This method can be used to monitor small spectral changes in absorption by detecting fluorescence X-ray photons emitted through a longer-lived intermediate state (with respect to the core hole state), resulting in an almost background-free measurement with reduced spectral broadening that yields a high-resolution absorption spectrum.[38−44] FeRu has a MMCT transition in the near IR region of the ultraviolet−visible (UV−vis) spectrum (λ_{MMCT} = 961 nm). Excitation into this broad band initiates an intramolecular charge transfer from the Fe to the Ru atom. Transient optical experiments have reported an ultrafast back electron transfer (BET) time of 89 ± 10 fs, and time-resolved Kβ emission reported a BET of 62 ± 10 fs.[9,34] Two-dimensional vibrational electronic spectroscopy has shown that the MMCT is strongly coupled to the cyanide bridge stretching mode in FeRu,[12] and a recent ultrafast X-ray scattering experiment of aqueous FeRu discovered that coherent motions of the first solvation shell play an important role in the ultrafast BET dynamics.[34] While these experiments measure vibronic coupling and solute−solvent interactions, they are limited in their ability to measure the time-resolved, non-equilibrium electron delocalization, which is a key property governing electron transfer dynamics.[2,3,45,46] In this study, we use ultrafast HERFD-XANES measurements and perform a computational study of the excited-state transient XANES spectroscopy based on LR-TDDFT to study electron

https://doi.org/10.1021/acs.jpclett.1c03613
J. Phys. Chem. Lett. 2022, 13, 378−386

delocalization between the two metal centers in FeRu by directly probing the valency of the Fe atom immediately following a MMCT excitation.

To measure the time-resolved valency of FeRu in an aqueous solution, we performed an optical pump, HERFD-XANES probe experiment at the X-ray Pump Probe (XPP) endstation at LCLS as shown in Figure 1a.[47] The MMCT transition in FeRu is excited at 800 nm, and the HERFD-XANES measurement is performed by recording the X-ray emission intensity at the peak of the ground-state Kα_1 ($2p_{3/2} \rightarrow 1s$) emission line using a Rowland spectrometer. Further experimental details are provided in the Experimental Methods and sections 2 and 3 of the Supporting Information. To understand how signatures of the oxidation state and metal−ligand interactions are encoded in the HERFD-XANES spectra, we plot the ground-state XANES (Figure 1c) and HERFD-XANES (Figure 1d) spectra of FeRu and two model complexes, $K_4Fe^{II}(CN)_6$ and $K_3Fe^{III}(CN)_6$, in aqueous solution measured at a synchrotron. A comparison of the XANES and HERFD-XANES reveals a large decrease in background and a decrease in peak widths of the spectral features in the latter measurement. The XANES-HERFD measurement better isolates the fluorescence line of interest from the background, allowing for the detection of small changes in the XANES spectral features.

While the HERFD-XANES spectrum is dependent on the cross sections for both absorption and Kα_1 emission, the primary factor determining the energy dependence of the HERFD-XANES intensity is the variation of the absorption cross section for each incident energy. Therefore, we can associate each peak with an absorption transition.[44] The characteristics of the X-ray near edge spectra for Fe(II) and Fe(III) model complexes dissolved in water have been discussed extensively in the literature[36,48] and are summarized in Figure 1 as peaks A, B, and C. Briefly, both Fe(II) and Fe(III) cyanide complexes exhibit peaks B and C that correspond to excitations of electrons from the 1s Fe core orbital to the metal e_g and ligand π^* molecular orbitals, respectively. The A peak is present only in the Fe(III) complex and indicates the presence of a hole in the t_{2g} molecular orbital. Peak A serves as an important spectral marker for monitoring the oxidation state of the Fe atom. We also observe blue shifts of the B and C features by ∼0.5 and ∼2 eV, respectively, upon oxidation of the Fe(II) complex. The ground-state HERFD-XANES spectrum of FeRu shows peaks B and C, characteristic of an Fe(II) complex, at 7114 and 7117 eV, respectively. Figure S4 compares the experimental and calculated XANES spectra of FeRu in its electronic ground state. The ground-state XANES calculations, performed at the LR-TDDFT level, account for explicit solute−solvent interactions, which are necessary to capture the features of the experimental spectrum.

In Figure 2b, we present the transient HERFD-XANES measurement of FeRu to characterize the short-lived mixed valence excited state formed upon MMCT excitation. The transient signal is plotted as the difference between the excited- and ground-state HERFD-XANES spectra summed over the optical pump/X-ray jitter delays between −35 and 35 fs. This delay range was chosen to cover the initial MMCT excitation and accounting for the ∼62 fs lifetime of the excited state.[34] The data show that the B and C features shift to the blue to ∼7115 and ∼7119 eV, respectively. In addition, a new peak appears in the difference spectrum at ∼7113 eV. To relate the observed changes in the transient HERFD-XANES spectrum

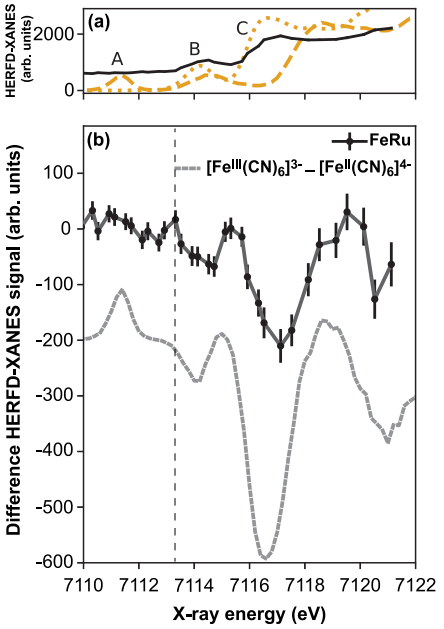

Figure 2. Transient HERFD-XANES signal. (a) Ground-state HERFD-XANES spectra of FeRu taken at LCLS (black solid), $[Fe^{II}(CN)_6]^{4-}$ taken at APS (yellow dotted), and $[Fe^{III}(CN)_6]^{3-}$ taken at APS (yellow dashed). Because the excited-state FeRu HERFD-XANES spectra are measured at the peak of the ground-state Kα_1 line, we also show the $[Fe^{III}(CN)_6]^{3-}$ HERFD-XANES spectra at the peak of the $[Fe^{II}(CN)_6]^{4-}$ Kα_1 line. (b) Difference spectra between the excited- and ground-state FeRu spectra shown as black circles in the bottom panels. To compare, the difference between the two model complexes is shown vertically offset as the gray dashed line. The difference of the model complex spectra is scaled by the excitation fraction of 0.25 and the difference in the concentration of the model complexes and FeRu.

to the mixed valency in the excited state of FeRu, we compare it to the difference between the ground-state HERFD-XANES spectra (Figure 2a) of the Fe(III) from the Fe(II) model complexes (gray dashed in Figure 2b). The model complex difference has been scaled to account for an excitation factor of 25% in the experiment as determined from a concurrent Kβ XES measurement.[34] The similarity in the dispersive line shapes for peaks B and C in the FeRu transient spectrum and the difference spectrum of the model complexes confirms that the MMCT from the Fe to the Ru results in an increase in the oxidation state of the Fe atom. Interestingly, the new feature at ∼7113 eV in the FeRu spectrum is significantly blue-shifted compared to the A feature of the Fe(III) complex at ∼7111 eV, suggesting that the transient Fe atom oxidation state is a fractional value between +2 and +3.

Developing a quantitative understanding of the experimental femtosecond XANES-HERFD data in Figure 2b required computations of the transient Fe K-edge XANES spectra at several points along the MMCT excited state (see section 4 of the Supporting Information for details). Briefly, excited-state geometries were computed by optimizing two clusters of the solvated FeRu complex (extracted from an equilibrated ground-state QM/MM calculation) on the MMCT surface. Transient Fe K-edge XANES computations were performed on these excited-state geometries by first converging the appropriate reference MMCT valence state in combination with the maximum overlap method implemented in NWChem.[49,50] The MMCT excited-state optimizations were

https://doi.org/10.1021/acs.jpclett.1c03613
J. Phys. Chem. Lett. 2022, 13, 378−386

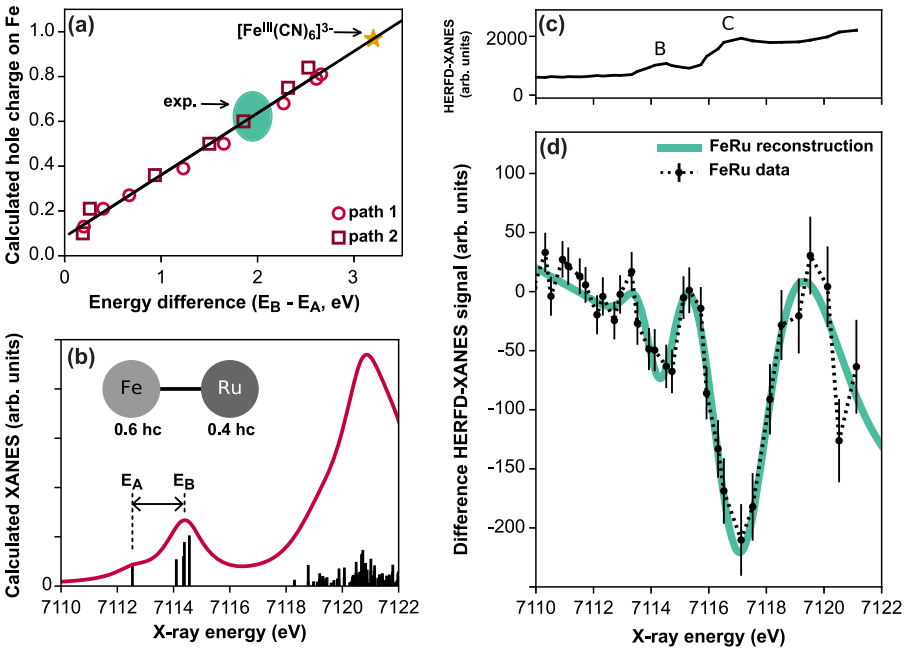

Figure 3. Computed and measured valence hole charge on the excited state of FeRu. (a) Computed Fe valence hole charge as a function of the A−B peak splitting in calculated transient Fe K-edge XANES spectra for two separate MMCT excited-state optimization paths (1 and 2). For comparison, the splitting between the A and B peaks for the ground-state experimental and computed $[Fe^{III}(CN)_6]^{3-}$ XANES spectrum is given by the yellow star (ref 36). (b) Computed excited-state XANES spectrum for a calculated Fe hole of 0.6. The arrows indicate the positions of the calculated A and B peaks used to construct the linear relationship in panel a. (c) Ground-state HERFD-XANES spectra of FeRu taken at LCLS. (d) Experimental difference spectrum between the excited- and ground-state FeRu XANES-HERFD spectra shown as black circles in the bottom panels. To measure the A and B peak positions, we reconstruct the difference spectrum using the ground-state FeRu spectrum, resulting in a measured A−B peak splitting of 1.9 ± 0.4 eV. The corresponding experimental measurement of the valence hole charge on FeRu using the spectral ruler in Figure 3a is shown as the green oval with the uncertainty given by its size.

performed with LR-TDDFT gradients,[51] while the XANES calculations were performed with the restricted excitation window LR-TDDFT approach,[52] including higher-order contributions to the oscillator strengths to capture the quadrupolar nature of the pre-edge transitions at the Fe K-edge. The computed XANES spectra at various points along the MMCT excited state from one representative optimization path are plotted in Figure S10. These points correspond to different excited-state valence hole charges on the Fe atom (given by the Mulliken and Löwdin populations). The calculated excited-state XANES spectra corresponding to different valence hole charges on the Fe atom reveal differences in the energy separation of peaks A and B. For each valence hole charge, the computed A peak energy is given by the lowest-energy transition, and the computed B peak energy is given by the broadened B peak transitions [E_B−E_A (Figure 3b)]. As shown in Figure 3a, we find a nearly linear relation between the energy difference of the A and B peaks with the Fe valence hole charge. Additionally, we note that the experimentally measured and calculated peak separation of model complex $[Fe^{III}(CN)_6]^{3-}$,[36] shown with a yellow star, also lies on the calculated linear line in Figure 3a. The physical interpretation of the calculated linear relationship between the Fe valence hole charge and the peak separation in the XANES spectra can be explained by noting that the crystal field splitting is approximately proportional to the magnitude of the dipole on the MMCT. Furthermore, the energy separation is proportional to the charge difference between the two metal centers as the system evolves on the MMCT state, given that the very short lifetime of the MMCT state (~62 fs) precludes any significant structural rearrangement.[34] This allows us to use this linear relation as a spectral ruler for determining the Fe valence hole charge. In Figure 3b, we show the computed excited-state XANES spectrum corresponding to the excited-state structure with a computed Fe valence hole charge of 0.6. We note that the structure corresponding to the experimentally determined value of the valence hole charge on Fe is an intermediate structure along the optimization path. This can be attributed to the slight underestimation of the energy of the charge transfer state at the level of theory used in these calculations (see Figure S2).

We use the computed linear relationship between the valence hole charge on the Fe atom and the A−B splitting to estimate the experimental valence hole charge on the Fe atom after the MMCT excitation. To extract the experimentally measured A−B splitting, we fit the difference spectrum using a function constructed from the difference of Gaussians at each A, B, and C peak for the excited-state spectrum and another sum of Gaussians for the ground-state spectrum, scaled to the excitation fraction of 0.25 determined in ref 34. To reduce the number of fit parameters, we use the peak positions, amplitudes, and widths of the ground-state B and C peaks determined by fitting two Gaussians and an error function to approximate the absorption edge to the FeRu ground-state XANES-HERFD spectrum. We also include a linear background to approximate the difference between the excited-state and ground-state absorption edges. At energies near the A and B peaks, this approximation is valid because the peak amplitudes are greater than or similar to the magnitude of the absorption edge. However, at higher photon energies, the amplitude of the absorption edge is larger than the C peak, invalidating the approximation. For this reason, the linear

https://doi.org/10.1021/acs.jpclett.1c03613
J. Phys. Chem. Lett. 2022, 13, 378−386

background approximation breaks down and the position and amplitude of the excited C peak are likely inaccurate. It would be possible to add higher-order terms to the background function. However, because we are interested in fitting only the A and B peaks, doing so unnecessarily adds additional terms to the fit, which could lead to an overfitting of the data. This is a particular risk in this case given the low resolution of the signal. We also note a feature near 7111 eV with an amplitude similar to that of the fitted A peak. An A peak in this region would result in a >3 eV splitting between the A and B peaks, which corresponds to a valence hole charge of >1. This is unphysical, and we therefore eliminate this possibility. Section 3.5 of the Supporting Information details the fit values, and the final reconstruction is shown as the thick green line in Figure 3. The final excited-state A and B peak positions are 7113.8 and 7115.7 eV, respectively.

Applying the linear relationship found between the calculated valence hole charges and A−B peak splitting, we estimate that the valence hole charge on the Fe atom over the time duration of our transient measurement is 0.6 ± 0.2. This valence hole charge value indicates that the charge is relatively delocalized across the Fe and Ru atoms. To show pictorially how the charge delocalization in the MMCT excited state is encoded in the Fe K-edge XANES spectra, we plot the transition densities associated with peak A in the calculated Fe K-edge XANES spectra of FeRu. For the case of the 0.1 Fe valence hole charge corresponding to the FeRu ground state, the transition density for peak A is localized on the Fe atom (Figure 4a). In contrast, the transition density for peak A is

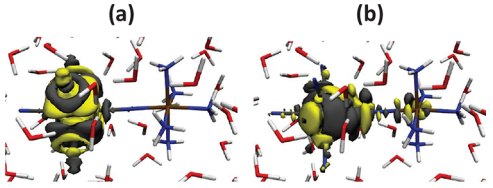

Figure 4. Transition density plots for peak A in the calculated FeRu XANES spectra at the Fe K-edge. The negative density is colored gray, while the positive density is colored yellow. (a) Peak A transition for the density for an optimized cluster corresponding to a 0.1 Fe valence hole charge on the ground state. (b) Peak A transition density for an optimized solvated cluster on the MMCT excited state corresponding to a 0.60 Fe valence hole charge.

shared between the bridging cyanide ligand and the Ru atom when the valence hole charge is 0.6 on the Fe atom (Figure 4b), providing a view of the local electronic structure of the experimentally measured MMCT excited state of FeRu with a lifetime of ∼65 fs.

The experimentally determined value of 0.6 valence hole charge on Fe using the spectroscopic ruler (Figure 3a) indicates that the short-lived MMCT excited state is more delocalized than the ground state in FeRu. Previous transient optical and IR experiments have determined time scales of the back electron transfer and the subsequent excitation of the high-frequency cyanide stretching modes in the non-equilibrium ground state. However, those experiments have been unable to measure the electronic character of the short-lived MMCT state in FeRu. This experiment and the plotted transition densities in Figure 4 showing electron delocalization across the cyanide bridging ligand connect with previously measured 2D VE spectra of FeRu in formamide where the vibronic coupling between the MMCT excitation and the cyanide stretching frequencies was strongest for the bridging mode.[12−13]

Our measurement of the Fe valence hole charge demonstrates how time-resolved HERFD-XANES spectroscopy combined with novel excited-state calculations can provide detailed information about the electron density in excited-state mixed valence metal complexes. With further XFEL enhancements, we expect that time-resolved HERFD-XANES demonstrated here will become an important tool for studying electron delocalization under non-equilibrium conditions. In particular, the ability to measure time-evolving HERFD-XANES spectra in the first 100 fs following optical excitation will provide key insights into electron transfer mechanisms and accompanying dynamics in complex molecular systems in realistic environments

EXPERIMENTAL METHODS

As shown in Figure 1a, 30 mM aqueous FeRu is introduced into the experiment via a 50 μm round jet. A 4 μJ, 40 fs full width at half-maximum (fwhm), 800 nm laser pulse with a 100−120 μm focus excites FeRu to the MMCT state. This pulse intensity is within the linear excitation regime, as determined by Kβ emission in ref 34, which was measured in concert with this experiment. The excited state is probed with time-overlapped 45 fs fwhm X-ray pulses at 120 Hz. The incident X-ray energy is scanned below the Fe K-edge using a 1 eV bandwidth Si(111) channel-cut monochromator, reducing the X-ray flux to 10^{10} photons per pulse with a 20−25 μm focus. For each pump probe event, the time delay between the laser and X-ray pulses is measured using the XPP timing tool.[47,53]

The HERFD-XANES measurement is performed by recording the X-ray emission intensity at the peak of the ground-state Kα_1 emission line using a Rowland monochromatic analyzer crystal and image area detector with a 0.4 eV resolution while scanning the incoming X-ray photon energy. The alignment of the spectrometer to the Kα_1 line is verified in Figure S6. The spectrometer intensity is then normalized to the pulse intensity as described in Section 3.2 of the Supporting Information. Similar measurements of FeRu and two model complexes, $K_4Fe^{II}(CN)_6$ and $K_3Fe^{III}(CN)_6$, were taken at beamline 7-ID-D at the Advanced Photon Source (APS) at Argonne National Laboratory using the same conditions described previously.[36]

COMPUTATIONAL METHODS

All ground- and excited-state calculations for this study were performed with the NWChem computational chemistry program.[49,50] We first performed ground-state QM/MM calculations on FeRu. Next, solvated clusters (≈238 atoms) were extracted (well-separated in time) from the equilibrated ground-state QM/MM trajectories by centering the FeRu complex as well as a 4 Å thick shell of explicit water molecules surrounding the complex. These representative clusters are sufficiently large to capture the spectral features compared with experiment (see Figures S1, S2, and S4). Two independent clusters were considered, and LR-TDDFT-based optimizations[51] on the MMCT excited state were performed starting from the Franck−Condon point. Due to the cost of the LR-TDDFT excited-state optimizations on these large solvated clusters, only two optimization paths (1 and 2) using the two clusters were performed. To track the excited-state valence

https://doi.org/10.1021/acs.jpclett.1c03613
J. Phys. Chem. Lett. 2022, 13, 378−386

hole charges as the system evolved along the MMCT surface, Mulliken and Löwdin population analyses were performed on the excited-state density, and transient Fe K-edge XANES spectra were calculated. For the excited-state XANES calculations, the appropriate reference MMCT valence state was first converged in combination with the maximum overlap method for the excited-state structures. The reference orbitals were then used for the subsequent Fe K-edge XANES calculations on these structures. The XANES calculations were performed with the restricted excitation window LR-TDDFT approach,[52] including higher-order contributions to the oscillator strengths, to capture the quadrupolar nature of the pre-edge transitions at the Fe K-edge. Further details of the calculations, including ground-state QM/MM, basis sets, and exchange correlation, are given in section 4 of the Supporting Information.

■ ASSOCIATED CONTENT

Supporting Information

The Supporting Information is available free of charge at https://pubs.acs.org/doi/10.1021/acs.jpclett.1c03613.

Materials; ground-state IR, UV−vis, XANES, and HERFD-XANES spectra; details of data analysis of femtosecond HERFD-XANES; and a complete description of the computational work (PDF)

■ AUTHOR INFORMATION

Corresponding Authors

Niranjan Govind − *Physical Sciences Division, Physical and Computational Sciences Directorate, Pacific Northwest National Laboratory, Richland, Washington 99352, United States;* orcid.org/0000-0003-3625-366X; Email: niri.govind@pnnl.gov

Munira Khalil − *Department of Chemistry, University of Washington, Seattle, Washington 98195, United States;* orcid.org/0000-0002-6508-4124; Email: mkhalil@uw.edu

Authors

Chelsea Liekhus-Schmaltz − *Department of Chemistry, University of Washington, Seattle, Washington 98195, United States*

Zachary W. Fox − *Department of Chemistry, University of Washington, Seattle, Washington 98195, United States*

Amity Andersen − *Environmental Molecular Sciences Laboratory, Earth and Biological Sciences Directorate, Pacific Northwest National Laboratory, Richland, Washington 99352, United States;* orcid.org/0000-0002-6529-0905

Kasper S. Kjaer − *Stanford PULSE Institute, SLAC National Accelerator Laboratory, Menlo Park, California 94025, United States; Department of Physics, Technical University of Denmark, 2800 Kongens Lyngby, Denmark*

Roberto Alonso-Mori − *Linac Coherent Light Source, SLAC National Accelerator Laboratory, Menlo Park, California 94025, United States*

Elisa Biasin − *Stanford PULSE Institute, SLAC National Accelerator Laboratory, Menlo Park, California 94025, United States;* Present Address: E.B.: Physical Sciences Division, Physical and Computational Sciences Directorate, Pacific Northwest National Laboratory, Richland, WA 99352; orcid.org/0000-0002-7276-4224

Julia Carlstad − *Department of Chemistry, University of Washington, Seattle, Washington 98195, United States;* Present Address: J.C. and J.D.G.: Department of Chemistry, University of California, Berkeley, Berkeley, CA 94720-1462.

Matthieu Chollet − *Linac Coherent Light Source, SLAC National Accelerator Laboratory, Menlo Park, California 94025, United States*

James D. Gaynor − *Department of Chemistry, University of Washington, Seattle, Washington 98195, United States;* Present Address: J.C. and J.D.G.: Department of Chemistry, University of California, Berkeley, Berkeley, CA 94720-1462.; orcid.org/0000-0001-5253-8142

James M. Glownia − *Linac Coherent Light Source, SLAC National Accelerator Laboratory, Menlo Park, California 94025, United States*

Kiryong Hong − *Ultrafast X-ray Science Laboratory, Chemical Sciences Division, Lawrence Berkeley National Laboratory, Berkeley, California 94720, United States;* Present Address: K.H.: Gas Metrology Group, Division of Chemical and Biological Metrology, Korea Research Institute of Standards and Science, Daejeon 34113, Republic of Korea; orcid.org/0000-0002-3590-3635

Thomas Kroll − *SSRL, SLAC National Accelerator Laboratory, Menlo Park, California 94025, United States*

Jae Hyuk Lee − *Ultrafast X-ray Science Laboratory, Chemical Sciences Division, Lawrence Berkeley National Laboratory, Berkeley, California 94720, United States;* Present Address: J.H.L.: Pohang Accelerator Laboratory, Pohang 37673, Republic of Korea

Benjamin I. Poulter − *Department of Chemistry, University of Washington, Seattle, Washington 98195, United States*

Marco Reinhard − *Stanford PULSE Institute, SLAC National Accelerator Laboratory, Menlo Park, California 94025, United States*

Dimosthenis Sokaras − *SSRL, SLAC National Accelerator Laboratory, Menlo Park, California 94025, United States*

Yu Zhang − *Department of Chemistry and Department of Physics & Astronomy, University of California, Irvine, California 94025, United States;* Present Address: Y.Z.: Q-Chem Inc., Pleasanton, CA 94588

Gilles Doumy − *Chemical Sciences and Engineering Division, Argonne National Laboratory, Lemont, Illinois 60439, United States;* orcid.org/0000-0001-8672-4138

Anne Marie March − *Chemical Sciences and Engineering Division, Argonne National Laboratory, Lemont, Illinois 60439, United States;* orcid.org/0000-0003-2961-1246

Stephen H. Southworth − *Chemical Sciences and Engineering Division, Argonne National Laboratory, Lemont, Illinois 60439, United States*

Shaul Mukamel − *Department of Chemistry and Department of Physics & Astronomy, University of California, Irvine, California 94025, United States;* orcid.org/0000-0002-6015-3135

Amy A. Cordones − *Stanford PULSE Institute, SLAC National Accelerator Laboratory, Menlo Park, California 94025, United States;* orcid.org/0000-0001-9897-5380

Robert W. Schoenlein − *Stanford PULSE Institute, SLAC National Accelerator Laboratory, Menlo Park, California 94025, United States; Linac Coherent Light Source, SLAC National Accelerator Laboratory, Menlo Park, California 94025, United States*

https://doi.org/10.1021/acs.jpclett.1c03613
J. Phys. Chem. Lett. 2022, 13, 378−386

Complete contact information is available at:
https://pubs.acs.org/10.1021/acs.jpclett.1c03613

Notes

The authors declare no competing financial interest.

■ ACKNOWLEDGMENTS

This work was supported by the U.S. Department of Energy, Office of Science, Basic Energy Sciences, Chemical Sciences, Geosciences and Biosciences Division, under Awards DE-SC0012450 (Z.W.F., J.C., J.D.G., Y.Z., S.M., and M.K.), KC-030105066418 (N.G.), DE-SC0019277 (C.L.-S. and M.K.), DE-FG02-04ER15571 (S.M.), and KC-030105172685 (N.G.) and Contracts DE-AC02-76SF00515 (E.B., K.S.K., K.H., J.H.L., M.R., R.W.S., and A.C.) and DE-AC02-06CH11357 (G.D., A.M.M., and S.H.S.). J.D.G. acknowledges support by the NSF GRFP (DGE-1256082). B.I.P. acknowledges support by the NSF GRFP (DGE-1762114). This research used resources of the Advanced Photon Source, a U.S. Department of Energy (DOE) Office of Science User Facility operated for the DOE Office of Science by Argonne National Laboratory under Contract DE-AC02-06CH11357. Use of the Linac Coherent Light Source (LCLS), SLAC National Accelerator Laboratory, is supported by the U.S. Department of Energy, Office of Science, Office of Basic Energy Sciences, under Contract DE-AC02-76SF00515. This research benefited from computational resources provided by EMSL, a DOE Office of Science User Facility sponsored by the Office of Biological and Environmental Research and located at PNNL. PNNL is operated by Battelle Memorial Institute for the DOE under DOE Contract DE-AC05-76RL1830. This research also used resources of the National Energy Research Scientific Computing Center (NERSC), a DOE Office of Science User Facility operated under Contract DE-AC02-05CH11231.

■ REFERENCES

(1) Creutz, C.; Taube, H. Direct approach to measuring the Franck-Condon barrier to electron transfer between metal ions. *J. Am. Chem. Soc.* **1969**, *91* (14), 3988−3989.
(2) Kubiak, C. P. Inorganic Electron Transfer: Sharpening a Fuzzy Border in Mixed Valency and Extending Mixed Valency across Supramolecular Systems. *Inorg. Chem.* **2013**, *52* (10), 5663−5676.
(3) Demadis, K. D.; Hartshorn, C. M.; Meyer, T. J. The Localized-to-Delocalized Transition in Mixed-Valence Chemistry. *Chem. Rev.* **2001**, *101* (9), 2655−2686.
(4) Robin, M. B.; Day, P. Mixed Valence Chemistry: A Survey and Classification. *Adv. Inorg. Chem. Radiochem.* **1968**, *10*, 247−422.
(5) Wang, C.; Mohney, B. K.; Akhremitchev, B. B.; Walker, G. C. Ultrafast Infrared Spectroscopy of Vibrational States Prepared by Photoinduced Electron Transfer in $(CN)_5FeCNRu(NH_3)^{5-}$. *J. Phys. Chem. A* **2000**, *104* (18), 4314−4320.
(6) Tominaga, K.; Kliner, D. A. V.; Johnson, A. E.; Levinger, N. E.; Barbara, P. F. Femtosecond experiments and absolute rate calculations on intervalence electron transfer of mixed-valence compounds. *J. Chem. Phys.* **1993**, *98* (2), 1228−1243.
(7) Tivanski, A. V.; Wang, C.; Walker, G. C. Vibrational Mode Coupling to Ultrafast Electron Transfer in $[(CN)_5OsCNRu(NH_3)_5]^-$ Studied by Femtosecond Infrared Spectroscopy. *J. Phys. Chem. A* **2003**, *107* (43), 9051−9058.
(8) Slenkamp, K. M.; Lynch, M. S.; Van Kuiken, B. E.; Brookes, J. F.; Bannan, C. C.; Daifuku, S. L.; Khalil, M. Investigating vibrational anharmonic couplings in cyanide-bridged transition metal mixed valence complexes using two-dimensional infrared spectroscopy. *J. Chem. Phys.* **2014**, *140* (8), 084505.
(9) Reid, P. J.; Silva, C.; Barbara, P. F.; Karki, L.; Hupp, J. T. Electronic Coherence, Vibrational Coherence, and Solvent Degrees of Freedom in the Femtosecond Spectroscopy of Mixed-Valence Metal Dimers in H2O and D2O. *J. Phys. Chem.* **1995**, *99* (9), 2609−2616.
(10) Lynch, M. S.; Van Kuiken, B. E.; Daifuku, S. L.; Khalil, M. On the Role of High-Frequency Intramolecular Vibrations in Ultrafast Back-Electron Transfer Reactions. *J. Phys. Chem. Lett.* **2011**, *2* (17), 2252−2257.
(11) Lynch, M. S.; Slenkamp, K. M.; Khalil, M. Probing non-equilibrium vibrational relaxation pathways of highly excited C≡N stretching modes following ultrafast back-electron transfer. *J. Chem. Phys.* **2012**, *136* (24), 241101.
(12) Fox, Z. W.; Blair, T. J.; Khalil, M. Determining the Orientation and Vibronic Couplings between Electronic and Vibrational Coordinates with Polarization-Selective Two-Dimensional Vibrational-Electronic Spectroscopy. *J. Phys. Chem. Lett.* **2020**, *11* (4), 1558−1563.
(13) Courtney, T. L.; Fox, Z. W.; Estergreen, L.; Khalil, M. Measuring Coherently Coupled Intramolecular Vibrational and Charge-Transfer Dynamics with Two-Dimensional Vibrational-Electronic Spectroscopy. *J. Phys. Chem. Lett.* **2015**, *6* (7), 1286−1292.
(14) Bressler, C.; Chergui, M. Ultrafast X-ray Absorption Spectroscopy. *Chem. Rev.* **2004**, *104* (4), 1781−1812.
(15) Gaffney, K. J. Capturing photochemical and photophysical transformations in iron complexes with ultrafast X-ray spectroscopy and scattering. *Chem. Sci.* **2021**, *12* (23), 8010−8025.
(16) Bergmann, U.; Kern, J.; Schoenlein, R. W.; Wernet, P.; Yachandra, V. K.; Yano, J. Using X-ray free-electron lasers for spectroscopy of molecular catalysts and metalloenzymes. *Nat. Rev. Phys.* **2021**, *3* (4), 264−282.
(17) Wernet, P. Chemical interactions and dynamics with femtosecond X-ray spectroscopy and the role of X-ray free-electron lasers. *Philos. Trans A Math Phys. Eng. Sci.* **2019**, *377* (2145), 20170464.
(18) Kraus, P. M.; Zurch, M.; Cushing, S. K.; Neumark, D. M.; Leone, S. R. The ultrafast X-ray spectroscopic revolution in chemical dynamics. *Nat. Rev. Chem.* **2018**, *2* (6), 82−94.
(19) Chergui, M.; Collet, E. Photoinduced structural dynamics of molecular systems mapped by time-resolved X-ray methods. *Chem. Rev. (Washington, DC, U. S.)* **2017**, *117* (16), 11025−11065.
(20) Chen, L. X. Ultrafast photochemical reaction trajectories revealed by X-ray transient absorption spectroscopy using X-ray free electron laser sources. *RSC Energy Environ. Ser.* **2017**, *18*, 201−224.
(21) Seddon, E. A.; Clarke, J. A.; Dunning, D. J.; Masciovecchio, C.; Milne, C. J.; Parmigiani, F.; Rugg, D.; Spence, J. C. H.; Thompson, N. R.; Ueda, K.; Vinko, S. M.; Wark, J. S.; Wurth, W. Short-wavelength free-electron laser sources and science: a review. *Rep. Prog. Phys.* **2017**, *80* (11), 115901.
(22) Huang, Z.; Kim, K.-J. Review of x-ray free-electron laser theory. *Phys. Rev. Spec. Top. Accel Beams* **2007**, *10* (3), 034801.
(23) Zhang, W.; Alonso-Mori, R.; Bergmann, U.; Bressler, C.; Chollet, M.; Galler, A.; Gawelda, W.; Hadt, R. G.; Hartsock, R. W.; Kroll, T.; Kjær, K. S.; Kubiček, K.; Lemke, H. T.; Liang, H. W.; Meyer, D. A.; Nielsen, M. M.; Purser, C.; Robinson, J. S.; Solomon, E. I.; Sun, Z.; Sokaras, D.; van Driel, T. B.; Vankó, G.; Weng, T.-C.; Zhu, D.; Gaffney, K. J. Tracking excited-state charge and spin dynamics in iron coordination complexes. *Nature* **2014**, *509* (7500), 345−348.
(24) Wernet, P.; Kunnus, K.; Josefsson, I.; Rajkovic, I.; Quevedo, W.; Beye, M.; Schreck, S.; Grübel, S.; Scholz, M.; Nordlund, D.; Zhang, W.; Hartsock, R. W.; Schlotter, W. F.; Turner, J. J.; Kennedy, B.; Hennies, F.; de Groot, F. M. F.; Gaffney, K. J.; Techert, S.; Odelius, M.; Föhlisch, A. Orbital-specific mapping of the ligand exchange dynamics of $Fe(CO)_5$ in solution. *Nature* **2015**, *520* (7545), 78−81.
(25) Vankó, G.; Bordage, A.; Pápai, M.; Haldrup, K.; Glatzel, P.; March, A. M.; Doumy, G.; Britz, A.; Galler, A.; Assefa, T.; Cabaret, D.; Juhin, A.; van Driel, T. B.; Kjær, K. S.; Dohn, A.; Møller, K. B.; Lemke, H. T.; Gallo, E.; Rovezzi, M.; Németh, Z.; Rozsályi, E.; Rozgonyi, T.; Uhlig, J.; Sundström, V.; Nielsen, M. M.; Young, L.; Southworth, S. H.; Bressler, C.; Gawelda, W. Detailed Character-

ization of a Nanosecond-Lived Excited State: X-ray and Theoretical Investigation of the Quintet State in Photoexcited $[Fe(terpy)_2]^{2+}$. *J. Phys. Chem. C* **2015**, *119* (11), 5888−5902.
(26) Shelby, M. L.; Lestrange, P. J.; Jackson, N. E.; Haldrup, K.; Mara, M. W.; Stickrath, A. B.; Zhu, D.; Lemke, H. T.; Chollet, M.; Hoffman, B. M.; Li, X.; Chen, L. X. Ultrafast Excited State Relaxation of a Metalloporphyrin Revealed by Femtosecond X-ray Absorption Spectroscopy. *J. Am. Chem. Soc.* **2016**, *138* (28), 8752−8764.
(27) Ogi, Y.; Obara, Y.; Katayama, T.; Suzuki, Y.-I.; Liu, S. Y.; Bartlett, N. C.-M.; Kurahashi, N.; Karashima, S.; Togashi, T.; Inubushi, Y.; Ogawa, K.; Owada, S.; Rubešová, M.; Yabashi, M.; Misawa, K.; Slavíček, P.; Suzuki, T. Ultraviolet photochemical reaction of $[Fe(III)(C_2O_4)_3]^{3-}$ in aqueous solutions studied by femtosecond time-resolved X-ray absorption spectroscopy using an X-ray free electron laser. *Struct. Dyn.* **2015**, *2* (3), 034901.
(28) Miller, N. A.; Deb, A.; Alonso-Mori, R.; Garabato, B. D.; Glownia, J. M.; Kiefer, L. M.; Koralek, J.; Sikorski, M.; Spears, K. G.; Wiley, T. E.; Zhu, D.; Kozlowski, P. M.; Kubarych, K. J.; Penner-Hahn, J. E.; Sension, R. J. Polarized XANES Monitors Femtosecond Structural Evolution of Photoexcited Vitamin B12. *J. Am. Chem. Soc.* **2017**, *139* (5), 1894−1899.
(29) Lemke, H. T.; Bressler, C.; Chen, L. X.; Fritz, D. M.; Gaffney, K. J.; Galler, A.; Gawelda, W.; Haldrup, K.; Hartsock, R. W.; Ihee, H.; Kim, J.; Kim, K. H.; Lee, J. H.; Nielsen, M. M.; Stickrath, A. B.; Zhang, W.; Zhu, D.; Cammarata, M. Femtosecond X-ray Absorption Spectroscopy at a Hard X-ray Free Electron Laser: Application to Spin Crossover Dynamics. *J. Phys. Chem. A* **2013**, *117* (4), 735−740.
(30) Kunnus, K.; Vacher, M.; Harlang, T. C. B.; Kjær, K. S.; Haldrup, K.; Biasin, E.; van Driel, T. B.; Pápai, M.; Chabera, P.; Liu, Y.; Tatsuno, H.; Timm, C.; Källman, E.; Delcey, M.; Hartsock, R. W.; Reinhard, M. E.; Koroidov, S.; Laursen, M. G.; Hansen, F. B.; Vester, P.; Christensen, M.; Sandberg, L.; Németh, Z.; Szemes, D. S.; Bajnóczi, É.; Alonso-Mori, R.; Glownia, J. M.; Nelson, S.; Sikorski, M.; Sokaras, D.; Lemke, H. T.; Canton, S. E.; Møller, K. B.; Nielsen, M. M.; Vankó, G.; Wärnmark, K.; Sundström, V.; Persson, P.; Lundberg, M.; Uhlig, J.; Gaffney, K. J. Vibrational wavepacket dynamics in Fe carbene photosensitizer determined with femtosecond X-ray emission and scattering. *Nat. Commun.* **2020**, *11* (1), 634.
(31) Kunnus, K.; Josefsson, I.; Rajkovic, I.; Schreck, S.; Quevedo, W.; Beye, M.; Weniger, C.; Grübel, S.; Scholz, M.; Nordlund, D.; Zhang, W.; Hartsock, R. W.; Gaffney, K. J.; Schlotter, W. F.; Turner, J. J.; Kennedy, B.; Hennies, F.; de Groot, F. M. F.; Techert, S.; Odelius, M.; Wernet, P.; Föhlisch, A. Identification of the dominant photochemical pathways and mechanistic insights to the ultrafast ligand exchange of $Fe(CO)_5$ to $Fe(CO)_4EtOH$. *Struct. Dyn.* **2016**, *3* (4), 043204.
(32) Haldrup, K.; Gawelda, W.; Abela, R.; Alonso-Mori, R.; Bergmann, U.; Bordage, A.; Cammarata, M.; Canton, S. E.; Dohn, A. O.; van Driel, T. B.; Fritz, D. M.; Galler, A.; Glatzel, P.; Harlang, T.; Kjær, K. S.; Lemke, H. T.; Møller, K. B.; Németh, Z.; Pápai, M.; Sas, N.; Uhlig, J.; Zhu, D.; Vankó, G.; Sundström, V.; Nielsen, M. M.; Bressler, C. Observing Solvation Dynamics with Simultaneous Femtosecond X-ray Emission Spectroscopy and X-ray Scattering. *J. Phys. Chem. B* **2016**, *120* (6), 1158−1168.
(33) Canton, S. E.; Kjær, K. S.; Vankó, G.; van Driel, T. B.; Adachi, S.-i.; Bordage, A.; Bressler, C.; Chabera, P.; Christensen, M.; Dohn, A. O.; Galler, A.; Gawelda, W.; Gosztola, D.; Haldrup, K.; Harlang, T.; Liu, Y.; Møller, K. B.; Németh, Z.; Nozawa, S.; Pápai, M.; Sato, T.; Sato, T.; Suarez-Alcantara, K.; Togashi, T.; Tono, K.; Uhlig, J.; Vithanage, D. A.; Wärnmark, K.; Yabashi, M.; Zhang, J.; Sundström, V.; Nielsen, M. M. Visualizing the non-equilibrium dynamics of photoinduced intramolecular electron transfer with femtosecond X-ray pulses. *Nat. Commun.* **2015**, *6* (1), 6359.
(34) Biasin, E.; Fox, Z. W.; Andersen, A.; Ledbetter, K.; Kjær, K. S.; Alonso-Mori, R.; Carlstad, J. M.; Chollet, M.; Gaynor, J. D.; Glownia, J. M.; Hong, K.; Kroll, T.; Lee, J. H.; Liekhus-Schmaltz, C.; Reinhard, M.; Sokaras, D.; Zhang, Y.; Doumy, G.; March, A. M.; Southworth, S. H.; Mukamel, S.; Gaffney, K. J.; Schoenlein, R. W.; Govind, N.; Cordones, A. A.; Khalil, M. Direct observation of coherent femtosecond solvent reorganization coupled to intramolecular electron transfer. *Nat. Chem.* **2021**, *13* (4), 343−349.
(35) Bokarev, S. I.; Kühn, O. Theoretical X-ray spectroscopy of transition metal compounds. *Wiley Interdiscip. Rev.: Comput. Mol. Sci.* **2020**, *10* (1), No. e1433.
(36) Ross, M.; Andersen, A.; Fox, Z. W.; Zhang, Y.; Hong, K.; Lee, J.-H.; Cordones, A.; March, A. M.; Doumy, G.; Southworth, S. H.; Marcus, M. A.; Schoenlein, R. W.; Mukamel, S.; Govind, N.; Khalil, M. Comprehensive Experimental and Computational Spectroscopic Study of Hexacyanoferrate Complexes in Water: From Infrared to X-ray Wavelengths. *J. Phys. Chem. B* **2018**, *122* (19), 5075−5086.
(37) Van Kuiken, B. E.; Valiev, M.; Daifuku, S. L.; Bannan, C.; Strader, M. L.; Cho, H.; Huse, N.; Schoenlein, R. W.; Govind, N.; Khalil, M. Simulating Ru L3-Edge X-ray Absorption Spectroscopy with Time-Dependent Density Functional Theory: Model Complexes and Electron Localization in Mixed-Valence Metal Dimers. *J. Phys. Chem. A* **2013**, *117* (21), 4444−4454.
(38) Tanaka, S.; Okada, K.; Kotani, A. Resonant X-Ray Emission Spectroscopy in Dy Compounds. *J. Phys. Soc. Jpn.* **1994**, *63* (7), 2780−2787.
(39) Müller, P.; Neuba, A.; Flörke, U.; Henkel, G.; Kühne, T. D.; Bauer, M. Experimental and Theoretical High Energy Resolution Hard X-ray Absorption and Emission Spectroscopy on Biomimetic Cu2S2 Complexes. *J. Phys. Chem. A* **2019**, *123* (16), 3575−3581.
(40) Heijboer, W. M.; Glatzel, P.; Sawant, K. R.; Lobo, R. F.; Bergmann, U.; Barrea, R. A.; Koningsberger, D. C.; Weckhuysen, B. M.; de Groot, F. M. F. Kβ-Detected XANES of Framework-Substituted FeZSM-5 Zeolites. *J. Phys. Chem. B* **2004**, *108* (28), 10002−10011.
(41) Hämäläinen, K.; Siddons, D. P.; Hastings, J. B.; Berman, L. E. Elimination of the inner-shell lifetime broadening in x-ray-absorption spectroscopy. *Phys. Rev. Lett.* **1991**, *67* (20), 2850−2853.
(42) Guo, M.; Prakash, O.; Fan, H.; de Groot, L. H. M.; Freyr Hlynsson, V.; Kaufhold, S.; Gordivska, O.; Velásquez, N.; Chabera, P.; Glatzel, P.; Wärnmark, K.; Persson, P.; Uhlig, J. HERFD-XANES probes of electronic structures of iron II/III carbene complexes. *Phys. Chem. Chem. Phys.* **2020**, *22* (16), 9067−9073.
(43) Bauer, M. HERFD-XAS and valence-to-core-XES: new tools to push the limits in research with hard X-rays? *Phys. Chem. Chem. Phys.* **2014**, *16* (27), 13827−13837.
(44) Lima, F. A.; Bjornsson, R.; Weyhermüller, T.; Chandrasekaran, P.; Glatzel, P.; Neese, F.; DeBeer, S. High-resolution molybdenum K-edge X-ray absorption spectroscopy analyzed with time-dependent density functional theory. *Phys. Chem. Chem. Phys.* **2013**, *15* (48), 20911−20920.
(45) Watzky, M. A.; Endicott, J. F.; Song, X.; Lei, Y.; Macatangay, A. Red-Shifted Cyanide Stretching Frequencies in Cyanide-Bridged Transition Metal Donor-Acceptor Complexes. Support for Vibronic Coupling. *Inorg. Chem.* **1996**, *35* (12), 3463−3473.
(46) Kaupp, M.; Renz, M.; Parthey, M.; Stolte, M.; Würthner, F.; Lambert, C. Computational and spectroscopic studies of organic mixed-valence compounds: where is the charge? *Phys. Chem. Chem. Phys.* **2011**, *13* (38), 16973.
(47) Glownia, J. M.; Gumerlock, K.; Lemke, H. T.; Sato, T.; Zhu, D.; Chollet, M. Pump-probe experimental methodology at the Linac Coherent Light Source. *J. Synchrotron Radiat.* **2019**, *26* (3), 685−691.
(48) Penfold, T. J.; Reinhard, M.; Rittmann-Frank, M. H.; Tavernelli, I.; Rothlisberger, U.; Milne, C. J.; Glatzel, P.; Chergui, M. X-ray Spectroscopic Study of Solvent Effects on the Ferrous and Ferric Hexacyanide Anions. *J. Phys. Chem. A* **2014**, *118* (40), 9411−9418.
(49) Aprà, E.; Bylaska, E. J.; de Jong, W. A.; Govind, N.; Kowalski, K.; Straatsma, T. P.; Valiev, M.; van Dam, H. J. J.; Alexeev, Y.; Anchell, J.; Anisimov, V.; Aquino, F. W.; Atta-Fynn, R.; Autschbach, J.; Bauman, N. P.; Becca, J. C.; Bernholdt, D. E.; Bhaskaran-Nair, K.; Bogatko, S.; Borowski, P.; Boschen, J.; Brabec, J.; Bruner, A.; Cauët, E.; Chen, Y.; Chuev, G. N.; Cramer, C. J.; Daily, J.; Deegan, M. J. O.; Dunning, T. H., Jr.; Dupuis, M.; Dyall, K. G.; Fann, G. I.; Fischer, S. A.; Fonari, A.; Früchtl, H.; Gagliardi, L.; Garza, J.; Gawande, N.;

https://doi.org/10.1021/acs.jpclett.1c03613
J. Phys. Chem. Lett. 2022, 13, 378−386

Ghosh, S.; Glaesemann, K.; Götz, A. W.; Hammond, J.; Helms, V.; Hermes, E. D.; Hirao, K.; Hirata, S.; Jacquelin, M.; Jensen, L.; Johnson, B. G.; Jónsson, H.; Kendall, R. A.; Klemm, M.; Kobayashi, R.; Konkov, V.; Krishnamoorthy, S.; Krishnan, M.; Lin, Z.; Lins, R. D.; Littlefield, R. J.; Logsdail, A. J.; Lopata, K.; Ma, W.; Marenich, A. V.; Martin del Campo, J.; Mejia-Rodriguez, D.; Moore, J. E.; Mullin, J. M.; Nakajima, T.; Nascimento, D. R.; Nichols, J. A.; Nichols, P. J.; Nieplocha, J.; Otero-de-la-Roza, A.; Palmer, B.; Panyala, A.; Pirojsirikul, T.; Peng, B.; Peverati, R.; Pittner, J.; Pollack, L.; Richard, R. M.; Sadayappan, P.; Schatz, G. C.; Shelton, W. A.; Silverstein, D. W.; Smith, D. M. A.; Soares, T. A.; Song, D.; Swart, M.; Taylor, H. L.; Thomas, G. S.; Tipparaju, V.; Truhlar, D. G.; Tsemekhman, K.; Van Voorhis, T.; Vázquez-Mayagoitia, Á.; Verma, P.; Villa, O.; Vishnu, A.; Vogiatzis, K. D.; Wang, D.; Weare, J. H.; Williamson, M. J.; Windus, T. L.; Woliński, K.; Wong, A. T.; Wu, Q.; Yang, C.; Yu, Q.; Zacharias, M.; Zhang, Z.; Zhao, Y.; Harrison, R. J. NWChem: Past, present, and future. *J. Chem. Phys.* **2020**, *152* (18), 184102.

(50) Valiev, M.; Bylaska, E. J.; Govind, N.; Kowalski, K.; Straatsma, T. P.; Van Dam, H. J. J.; Wang, D.; Nieplocha, J.; Apra, E.; Windus, T. L.; de Jong, W. NWChem: A comprehensive and scalable open-source solution for large scale molecular simulations. *Comput. Phys. Commun.* **2010**, *181* (9), 1477−1489.

(51) Silverstein, D. W.; Govind, N.; van Dam, H. J. J.; Jensen, L. Simulating One-Photon Absorption and Resonance Raman Scattering Spectra Using Analytical Excited State Energy Gradients within Time-Dependent Density Functional Theory. *J. Chem. Theory Comput.* **2013**, *9* (12), 5490−5503.

(52) Lopata, K.; Van Kuiken, B. E.; Khalil, M.; Govind, N. Linear-Response and Real-Time Time-Dependent Density Functional Theory Studies of Core-Level Near-Edge X-Ray Absorption. *J. Chem. Theory Comput.* **2012**, *8* (9), 3284−3292.

(53) Chollet, M.; Alonso-Mori, R.; Cammarata, M.; Damiani, D.; Defever, J.; Delor, J. T.; Feng, Y.; Glownia, J. M.; Langton, J. B.; Nelson, S.; Ramsey, K.; Robert, A.; Sikorski, M.; Song, S.; Stefanescu, D.; Srinivasan, V.; Zhu, D.; Lemke, H. T.; Fritz, D. M. The X-ray Pump-Probe instrument at the Linac Coherent Light Source. *J. Synchrotron Radiat.* **2015**, *22* (3), 503−507.

https://doi.org/10.1021/acs.jpclett.1c03613
J. Phys. Chem. Lett. 2022, 13, 378−386

SUPPORTING INFORMATION

Femtosecond X-ray Spectroscopy Directly Quantifies Transient Excited State Mixed Valency

Chelsea Liekhus-Schmaltz,[1] Zachary W. Fox,[1] Amity Andersen,[2] Kasper S. Kjaer,[3,4] Roberto Alonso-Mori,[5] Elisa Biasin,[3,||] Julia Carlstad,[1,⊥] Matthieu Chollet,[5] James D. Gaynor,[1,⊥] James M. Glownia,[5] Kiryong Hong,[6,#] Thomas Kroll,[7] Jae Hyuk Lee,[6,▽] Benjamin I. Poulter,[1] Marco Reinhard,[3] Dimosthenis Sokaras,[7] Yu Zhang,[8,‡‡] Gilles Doumy,[9] Anne Marie March,[9] Stephen H. Southworth,[9] Shaul Mukamel,[8] Amy Cordones-Hahn,[3] Robert W. Schoenlein,[3,5] Niranjan Govind,[10] and Munira Khalil*[1]*

[1]Department of Chemistry, University of Washington, Seattle, WA ,98195 USA.

[2]Environmental Molecular Sciences Laboratory, Earth and Biological Sciences Directorate, Pacific Northwest National Laboratory, Richland, WA 99352, USA.

[3]Stanford PULSE Institute, SLAC National Accelerator Laboratory, Menlo Park, CA 94025, USA.

[4]Department of Physics, Technical University of Denmark, 2800 Kongens Lyngby, Denmark.

[5]Linac Coherent Light Source, SLAC National Accelerator Laboratory, Menlo Park, CA 94025, USA.

[6]Ultrafast X-ray Science Laboratory, Chemical Sciences Division, Lawrence Berkeley National Laboratory, Berkeley, CA 94720, USA

[7]SSRL, SLAC National Accelerator Laboratory, Menlo Park, CA 94025, USA

[8]Department of Chemistry, and Physics & Astronomy, University of California, Irvine, CA 94025, USA

[9]Chemical Sciences and Engineering Division, Argonne National Laboratory, Lemont, IL 92697, USA

[10]Physical Sciences Division, Physical and Computational Sciences Directorate, Pacific Northwest National Laboratory, Richland, WA 99352, USA

Corresponding Authors

niri.govind@pnnl.gov; mkhalil@uw.edu

Contents

1 Materials and Ground State Spectroscopy 3

1.1 Materials 3

1.2 Calculated and experimental ground state IR spectra in the CN stretching region of FeRu 4

1.3 Calculated and experimental ground state UV-Vis spectra of FeRu 4

1.4 Calculated and experimental ground state Fe K-edge XANES 5

2 Ground State HERFD-XANES 6

3 Femtosecond HERD-XANES of FeRu at LCLS 8

3.1 HERFD-XANES filter parameters 8

3.2 HERFD-XANES spectra definition 9

3.3 HERFD-XANES spectra spectrometer alignment 9

3.4 Bootstrapping 10

3.5 HERFD-XANES fit parameters 12

3.6 HERFD-XANES fits 13

4 Computations 14

4.1 Quantum-Mechanics/Molecular Mechanics (QM/MM) Simulations 14

4.2 LR-TDDFT Calculations 15

4.3 Valence hole charge 16

4.4 Molecular orbitals plots 17

References 18

1 Materials and Ground State Spectroscopy

1.1 Materials

Potassium ferrocyanide ($K_4Fe^{II}(CN)_6$) and ferricyanide ($K_3Fe^{III}(CN)_6$) compounds were purchased from Sigma Aldrich and used without further purification. The $[(CN)_5Fe^{II}–CN–Ru^{III}(NH_3)_5]Na$, (FeRu) sample used in this experiment was synthesized using literature methods with modifications previously described.[1-2]

1.2 Calculated and experimental ground state IR spectra in the CN stretching region of FeRu

The steady-state FTIR spectra of 12.5 mM FeRu solution was collected with a JASCO FT/IR 4100 instrument with a 50-micron pathlength. The spectral resolution was 2 cm^{-1}. The water background is subtracted from the spectrum. The comparison between the calculated and experimental IR spectra is shown in Fig. S1. The IR spectrum was computed using 20 clusters from the QM/MM calculations (see Section 4).

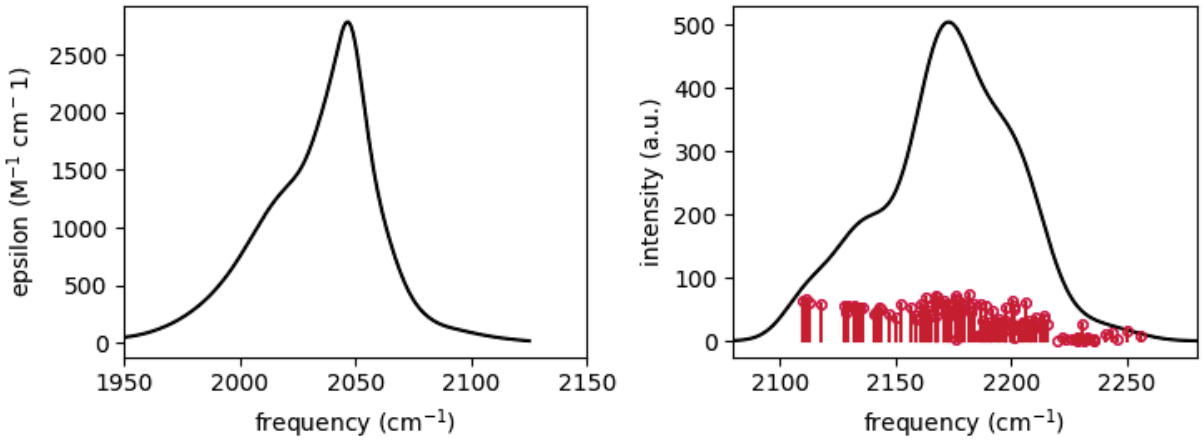

Figure S1: IR spectra. Shown in the left panel is the experimental FTIR spectra of FeRu. The right panel shows the unshifted broadened calculated IR spectra. The calculated spectrum is broadened by 10 cm^{-1}.

1.3 Calculated and experimental ground state UV-Vis spectra of FeRu

The steady-state ground state UV-Vis spectra of 12.5 mM FeRu solution was collected with a JASCO V630 spectrometer with a 50-micron pathlength. The spectral resolution was 0.5 nm. The broadened calculated UV-Vis spectrum is compared to the experimental UV-Vis spectrum in Fig. S2 with the transition density shown in Fig. S3.

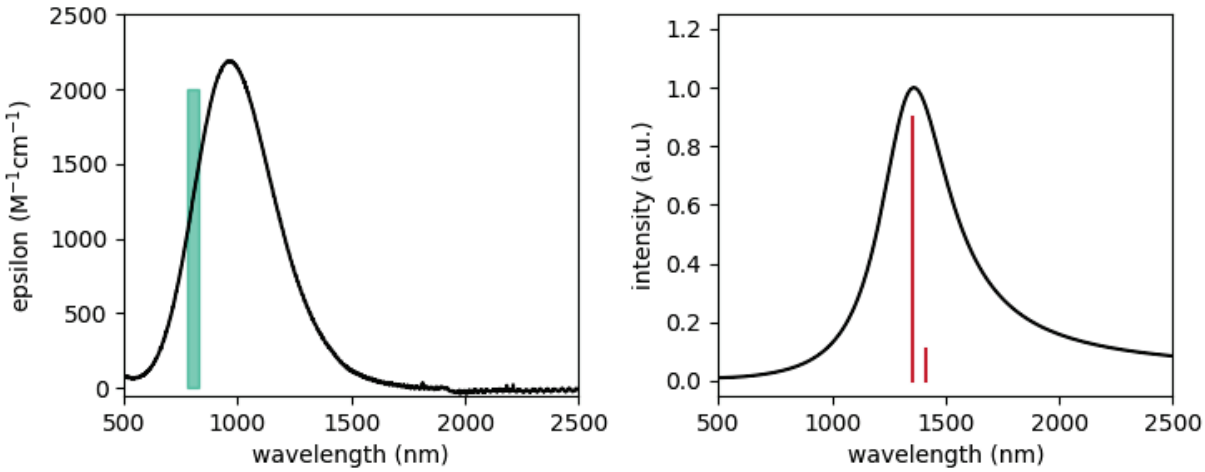

Figure S2: UV-Vis spectra. Shown in the left panel is the experimental UV-Vis spectra with the excitation region shown in the green rectangle. The right panel shows the unshifted, broadened calculated UV-Vis spectrum broadened by 0.25 eV.

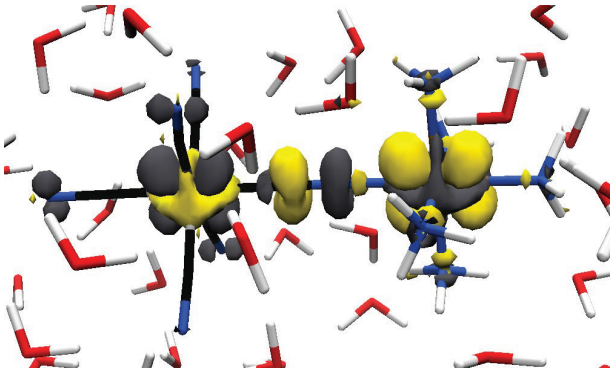

Figure S3: MMCT transition density. The electronic transition density associated with the strongest transition line in Fig. S2 is shown; the Fe atom being on the left and the Ru atom being on the right. An accumulation of charge is shown in yellow while a depletion in shown in gray.

1.4 Calculated and experimental ground state Fe K-edge XANES

The ground state XANES spectrum of 40 mM FeRu was measured at Beamline 10.3.2 of the Advanced Light Source at Lawrence Berkeley National Laboratory. Details of the sample cell have been given previously.[3] Details of the calculations are shown in Section 3.

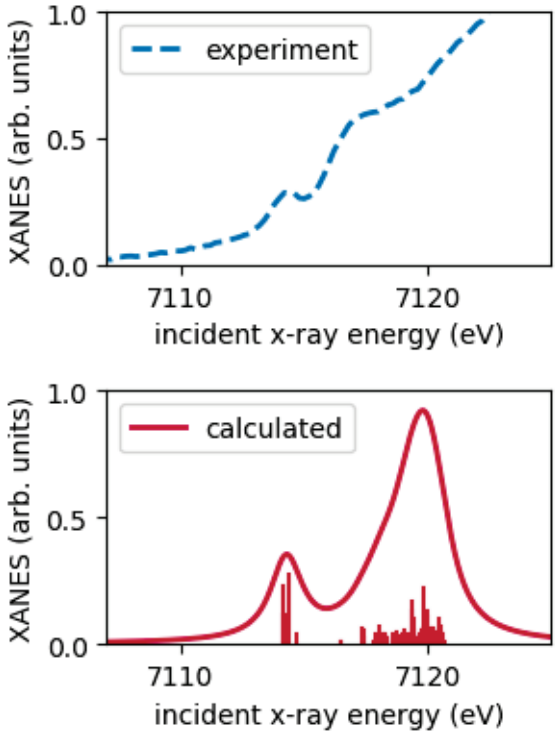

Figure S4: Fe K-edge XANES. Shown in the upper panel is the experimental Fe K-edge XANES of FeRu. The lower panel shows the broadened calculated Fe K-edge XANES. The calculated spectrum has been broadened by 1.5 eV and shifted by 144.7 eV.

2 Ground State HERFD-XANES

To explain in more detail the relation between the HERFD-XANES, XANES and RIXS spectra, we examine the full resonant inelastic X-ray scattering, RIXS, spectrum of the ($[Fe^{III}(CN)_6]^{3-}$) molecule here, which was taken at beamline 7-ID-D at the Advanced Photon Source (APS). The full RIXS spectrum of ($[Fe^{III}(CN)_6]^{3-}$) is shown in the upper left corner of Fig. S5. The processes involved in this measurement are shown in the lower right panel of Fig. S5, where the incoming X-ray photon core excites the molecule resulting in emission from the 2p orbitals, which is then spectrally resolved. Standard XANES measurements in partial fluorescence yield (PFY) mode are the projection of the RIXS plane onto the incident X-ray energy axis, as shown in the lower left panel. The width of the peaks in the XANES -PFY spectra are largely determined by the lifetime of the 1s hole.

The HERFD-XANES measurement is instead a slice along the RIXS plane along the peak of the emission spectra, as shown by the horizontal arrow in the upper left panel of Fig. S5. The

resulting spectra, shown in the upper right panel of Fig. S5, has narrower peaks, as their linewidth is largely determined by the 2p lifetime.

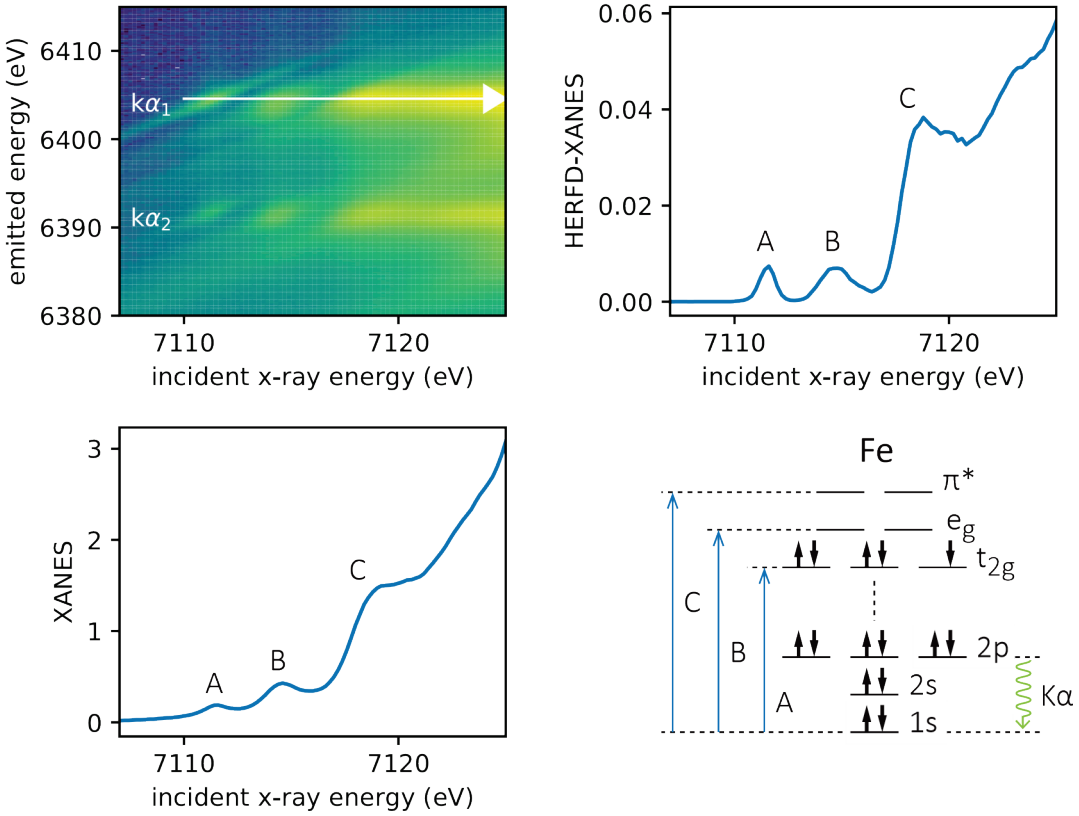

Figure S5: XANES vs HERFD-XANES comparison. In the upper left panel is the total RIXS plane of the ($[Fe^{III}(CN)_6]^{3-}$) molecule. A projection along the incident X-ray energy axis provides the standard XANES measurement, shown in the lower left panel. A cut along the emission peak is the HERFD-XANES spectra, shown in the upper right panel. Finally, the processes involved in measuring the RIXS spectra are shown in the lower right panel.

The ground state RIXS measurements of FeRu (30 mM) and the model complexes (100 mM) were taken at beamline 7-ID-D at the Advanced Photon Source (APS) at Argonne National Laboratory using the conditions described previously.[3]

The ground state HERFD-XANES spectra extracted from the RIXS measurements of FeRu, $[Fe^{II}(CN)_6]^{4-}$, and $[Fe^{III}(CN)_6]^{3-}$ are shown in Fig. S6 along with the calculated ground state XANES spectra of FeRu. There are two versions of the HERFD-XANES spectra of $[Fe^{III}(CN)_6]^{3-}$. The first version, labeled 'v1' in dotted blue, is given by the emission intensity at the peak of the $[Fe^{II}(CN)_6]^{4-}$ Kα_1 spectra. The second version, labeled 'v2' in solid blue, is given by the emission intensity at the peak of the $[Fe^{III}(CN)_6]^{3-}$ Kα_1 spectra, which is the standard method for finding the HERFD-XANES spectra. We compare these two versions because the excited state time resolved HERFD-XANES spectra uses the emission at the ground state Kα_1 maximum. We see that the

position of the peaks is not shifted significantly relative to the shifts caused by the change in oxidation state.

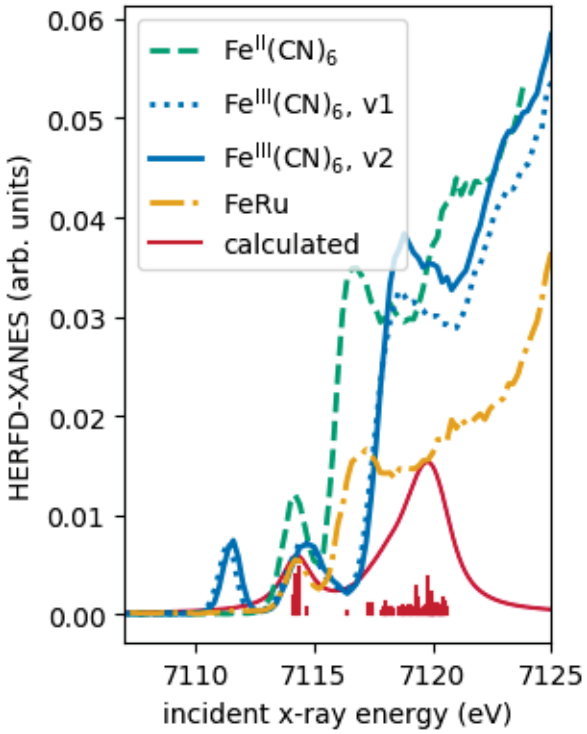

Figure S6: Ground state HERFD and XANES spectra. Ground state HERFD-XANES spectra of FeRu, FeII, FeIII taken at APS are show along with the ground state calculated XANES spectra of FeRu. The measurements are normalized by the integral of the full RIXS plane, and the calculation is scaled to match the B peak amplitude.

3 Femtosecond HERD-XANES of FeRu at LCLS

3.1 HERFD-XANES filter parameters

X-ray pulses from self-amplified spontaneous emission FEL sources lack temporal coherence between x-ray pulses. In addition, the liquid jet that contains our sample can fluctuate in its position and thickness. Therefore, we filter out dissimilar X-ray and jet shots with 8 different shot-to-shot measurements. Each of these values either report on the X-ray pulse characteristic, or the jet character. For each of these measurements, we filter out shots that are a certain number of standard deviations away from the median value, as shown in Table S1.

Table S1: Shot to shot filters for HERFD-XANES data. The filter parameters applied to the HERFD-XANES data are shown here. X-ray shots that are outside the specified number of standard deviations are removed from the analysis.

Value	number of STDs
X-ray intensity	2
Electron bunch energy	1
Integrated CSPAD signal	2
Integrated Rowland signal	2
TFY diode	2
Time Tool shift value	5
Time Tool signal amplitude	2
Time Tool signal width	2

In addition, we filter for a linear response between the x-ray intensity and the TFY signal. This filter is applied separately for each photon energy as well as for the un-pumped shots. The filter on this condition is relatively tight at 0.5 standard deviations from the linear regime.

3.2 HERFD-XANES spectra definition

The HERFD-XANES spectra reported in the main text, $S_{\mathrm{XANES}}(h\nu)$, at each incident photon energy, $h\nu$, is computed as the sum the of emission intensities measured by the Rowland spectrometer at the peak of the Kα_1 emission line, R_i, normalized by the sum of all x-ray intensities for each x-ray shot, I_i:

$$S_{XANES}(h\nu) = \frac{\sum_i R_i(h\nu)}{\sum_i I_i(h\nu)}$$

3.3 HERFD-XANES spectra spectrometer alignment

To ensure that the Rowland spectrometer has been properly tuned to the peak of the emission spectra so that we can straightforwardly interpret the HERFD-XANES spectra, we compare the ground state XANES spectra from the TFY diode to the ground state HERFD-XANES spectra. If the Rowland spectrometer is properly aligned, they will each have peaks in the same position. Figure S7 confirms that while there is a difference in shape for both spectra, their peak positions

still overlap. Of particular importance is the position of the B peak, which we use directly in our measurement, and is clearly well overlapped between the two measurements.

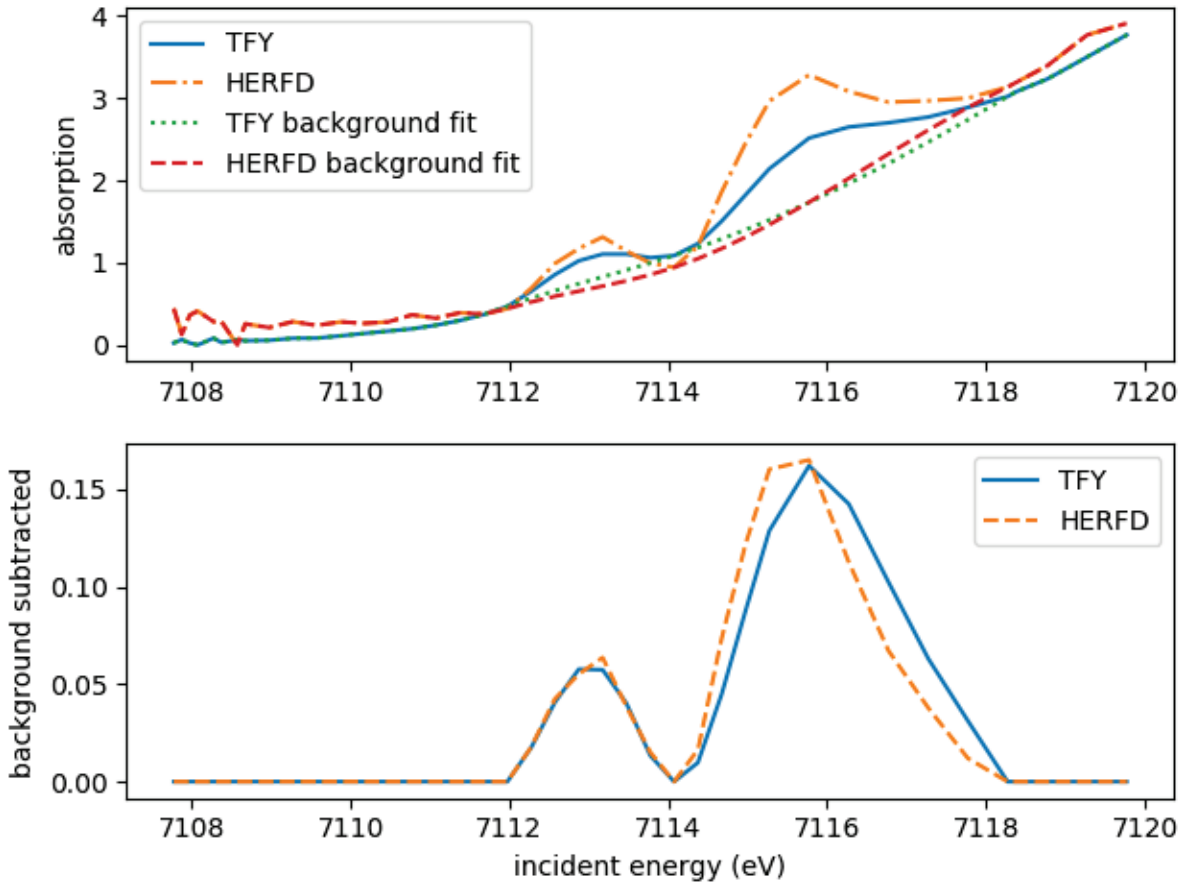

Figure S7: XANES and HERFD-XANES comparison. To confirm that we have appropriately set the Rowland spectrometer to the peak of the emission spectra so that we can straightforwardly use the HERFD-XANES measurement, we compare the XANES spectra from the TFY diode to the HERFD-XANES spectra. In the upper panel we see the raw spectra of both signals as well as the background fit, we subtract to get the lower panel. The background is spline interpolation of the spectra excluding the peaks. The peak position for both spectra can be compared in the lower panel, where we see that in fact the B and C peaks are in alignment.

3.4 Bootstrapping

Bootstrapping allows us to estimate the uncertainty of each data point.[4] A comprehensive guide to bootstrapping can be found in Ref. 4. In brief, bootstrapping is the technique of determining the desired measurement and its uncertainty by finding the mean and standard deviation of a collection of recalculated signals from a resampled data set. In more detail, each bootstrapped data set is

generated by resampling the raw data with replacement. In our case we have done this 1000 times to generate 1000 different bootstrapped data sets. We have used the same procedure for the XES and HERFD-XANES data, and we use the HERFD-XANES data as an example in this section. The bootstrapped data sets are then used to calculate 1000 different HERFD-XANES spectra, $S^{j}_{\mathrm{XANES}}(h\nu)$. The final reported value $S_{\mathrm{XANES}}(h\nu)$ is the mean of the bootstrapped data sets, and the uncertainty, $\Delta(h\nu)$ is the standard deviation. A figure showing the first 100 bootstrapped datasets can be seen in Fig. S8.

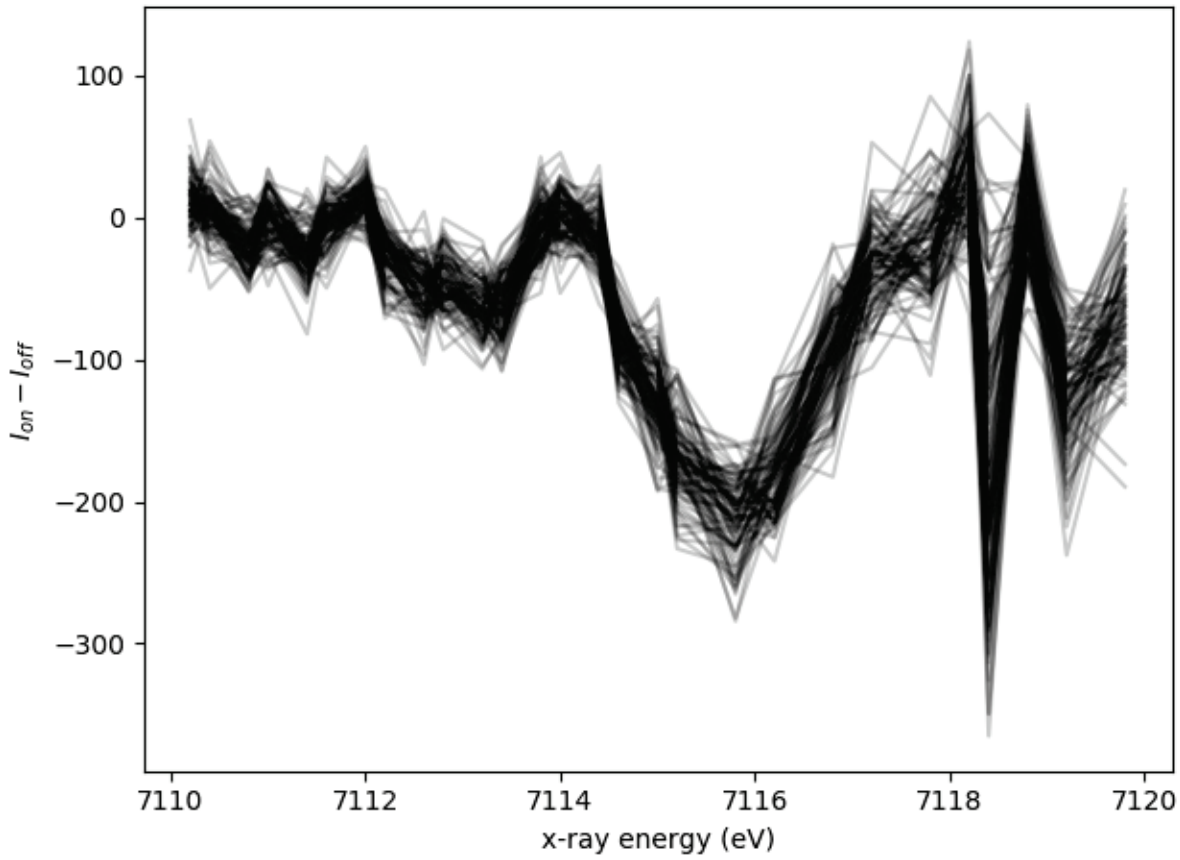

Figure S8: Bootstrapped dataset subset. To determine the uncertainty of our measurement, we use the bootstrapping technique to estimate the error. We create 1000 "bootstrapped" datasets by resampling our raw data with replacement 1000 times. We then perform our analysis to each of the datasets and use the mean and standard deviation of each point to report the final value and uncertainty of each data point respectively. Here, the first 100 bootstrap datasets are plotted on top of each other here. We identify the point at 7118.4 eV as having an unusually large amount of error and eliminate it from our dataset. This is because this energy bin contains only ≈ 4% the number of x-ray shots of other energy bins. Each of the other shots have ≈ 1500 shots in them.

3.5 HERFD-XANES fit parameters

The HERFD-XANES fit parameters used to determine the peak positions used in Fig. 3 of the main text are shown in Table S2 along with the corresponding fit equation. For completeness, Eq. 4 is the equation for a HERFD-XANES spectra with three peaks. For spectra with only two peaks, the amplitude of the A peak is set to zero.

$$F(x) = A_A * e^{-\frac{(x-x_{0,A})^2}{\sigma_A}} + A_B * e^{-\frac{(x-x_{0,B})^2}{\sigma_B}} + A_C * e^{-\frac{(x-x_{0,C})^2}{\sigma_C}} + F_0 + A_{edge} * \mathrm{erf}\left(\frac{x - x_{0,edge}}{\psi_{edge}}\right)$$

Table 2: HERFD-XANES fit parameters. Fit parameters of FeRu are shown here.

Parameter	Value
FeRu excited state measured at LCLS	
σ'_A	0.5 ± 0.7 eV^2
A'_A	60 ± 30
$x'_{0,A}$	7113.8 ± 0.3 eV
σ'_B	1.5 ± 1.3 eV^2
A'_B	120 ± 30
$x'_{0,B}$	7115.7 ± 0.3 eV
σ'_C	4 ± 4 eV^2
A'_C	130 ± 60
$x'_{0,C}$	7119 ± 0.4 eV
Difference linear background	
y_0	100,000 ± 50,000
A	-14 ± 7 eV^{-1}
FeRu ground state measured at LCLS	
σ_B	0.5 ± 0.3 eV^2
A_B	400 ± 100
$x_{0,B}$	7114.28 ± 0.09 eV
σ_C	2 ± 1 eV^2

A_C	1000 ± 500
$x_{0,C}$	7117.04 ± 0.08 eV
F_0	1600 ± 400
A_{edge}	1000 ± 400
ψ_{edge}	3 ± 4 eV
$x_{0,edge}$	7119.0 ± 0.7 eV

3.6 HERFD-XANES fits

The ground state FeRu HERFD-XANES measured at both LCLS and APS are shown here and fit to Eq. 4 with two peaks in Fig. 11. The ground state peak positions, widths, and amplitudes are used to fit the HERFD-XANES difference spectrum and extract the excited state. The extracted excited state is also compared to the calculated spectrum with a 0.6 valence hole charge on the Fe atom and on the ground state.

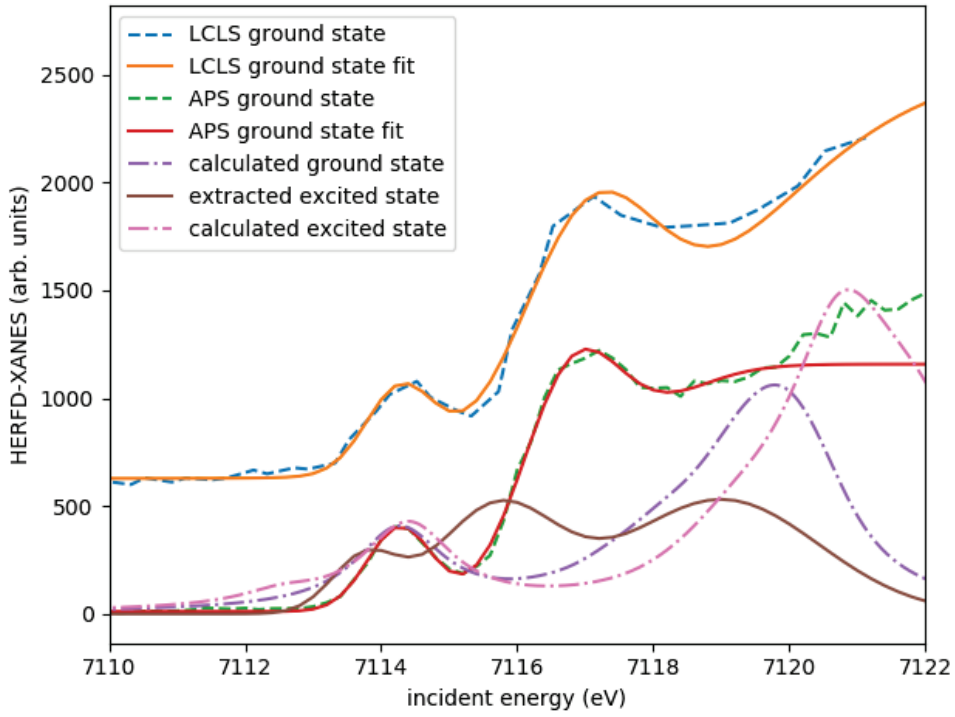

Figure S9: FeRu HERFD-XANES fits. The ground state FeRu data is shown as dashed lines. The fits for the ground state and the extracted excited states are shown as solid lines. The calculated ground and excited states are given by the dashed dotted lines.

4 Computations

All ground and excited state calculations were performed with the NWChem computational chemistry program.[5-6] These simulations were performed at the density functional theory (DFT) and time-dependent density functional theory (TDDFT) levels of theory. Our choice of DFT and TDDFT, which offer a good balance between accuracy and computational performance cost, was motivated by the sizes of the large explicitly solvated transition metal clusters considered in this study. We have successfully used the same approach in other studies, where we have shown the importance of explicit solvation, leading up to this work.[3, 7-8] Comparisons between experimental and calculated ground state IR, UV-Vis, and Fe K-edge XANES of FeRu are shown in Figs. S1, S2, and S4, respectively.

4.1 Quantum-Mechanics/Molecular Mechanics (QM/MM) Simulations

A QM/MM simulation of FeRu was first performed in the ground state.[3] The complex was solvated in a cubic water box of size 53 Å consisting of 4992 water molecules with a density of ~1 g/cm^3. A single potassium cation (K^+) was placed in the water solvent to charge balance the 1- charged FeRu complex. The FeRu complex was designated the quantum mechanics (QM) region, and the water molecules with the K^+ cation was designated the molecular mechanics (MM) region in subsequent QM/MM simulations. The classical force-field used for the water molecules was the extended single point charge water model (SPC/E) of Berendsen and co-workers.[9] The single K^+ cation was represented with the SPC/E-compatible K^+ force field of Joung and Cheatham.[10] For the QM region, van der Waals parameters for the C, N, and H atoms were obtained from the general AMBER force-field (GAFF) set.[11] The Fe and Ru atoms in the complex do not interact directly with the water solvent and are therefore assigned the Fe^{2+} (feo) van der Waals parameters of the CLAYFF forcefield of Cygan and co-workers to approximate the relatively short Fe/Ruligand van der Waals interactions.[12] Lorentz-Berthelot mixing and AMBER 1-4 rules for nonbonding interactions apply. Following the preparation of the solvated system and assignment of force-field parameters, the entire system was optimized.

The QM region was treated with DFT with the global hybrid PBE0 exchange-correlation density functional.[13-14] The 6-311G** basis set was used for the light atoms, H, C, and N,[15] and the Stuttgart scalar relativistic basis set and effective core potentials (ECP) were used for the Fe and Ru atoms.[16-17] The SHAKE algorithm[18] was applied to the water molecules to constrain the bond

lengths and bond angle, as prescribed by the SPC/E potential. The Coulombic interaction was set to 1.2 nm. The QM/MM interaction zone surrounding the complex was set to 2.0 nm. Geometry optimization was performed cyclically with a maximum of 10 QM region Broyden-Fletcher-Goldfarb-Shanno (BFGS) iterations followed by a maximum of 3000 MM region steepest-descent (SD) iterations. This cycle was repeated for a maximum of 5 times until convergence. Following optimization, QM/MM molecular dynamics were performed. Initially, the complex was held fixed and the water solvent was allowed to equilibrate over 10 ps with a time step of 2 fs and using the Berendsen thermostat[19] for NVT simulations at 298.15 K. After this initial equilibration, the complex was allowed to equilibrate with the solvent for 1 ps and a time step of 0.25 fs. Following 1 ps, QM/MM dynamics of the entire system was run for another 20 ps. These ground state calculations were performed with the NWChem QM/MM module.

4.2 LR-TDDFT Calculations

For the LR-TDDFT calculations of the FeRu complex, clusters were extracted from the equilibrated QM/MM trajectory. Clusters (≈ 238 atoms) were constructed by centering the transition metal complex center as well as a 4Å thick shell of explicit water molecules surrounding the complex. These clusters are sufficiently large to capture the ground state properties compared with experiment as seen in Figs. S1, S2, and S4 of the Supplementary Information. Excited state geometries were computed by optimizing these clusters on the MMCT surface and the transient Fe K-edge XANES computations were performed on these excited-state geometries by first converging the appropriate reference MMCT valence state in combination with the maximum overlap method implemented in NWChem. The MMCT excited state optimizations were performed with LR-TDDFT gradients,[20] while the XANES calculations were performed with the restricted excitation window LR-TDDFT approach,[21] including higher-order contributions to the oscillator strengths to capture the quadrupolar nature of the pre-edge transitions at the Fe K-edge. To follow the electron transfer, Mulliken and Löwdin populations were computed on the Fe and Ru atoms to track the excited state valence hole charges as the system evolved along the MMCT surface. For consistency, the PBE0 exchange-correlation density functional was also used in all the LR-TDDFT calculations,[13-14] along with the 6-311G** basis set for the light atoms, H, C, and N,[15] and the Stuttgart scalar relativistic basis set and effective core potentials (ECP) for Fe and

Ru,[16-17] respectively. The Fe K-edge XANES calculations were performed with the Fe atom represented with the all-electron Sapporo-TZP-2012 basis set.[22]

4.3 Valence hole charge

The computed spectrum for all of the valence hole charge values on the first optimization path, labeled 'path 1' in Fig. 3a is shown here. The splitting of the A and B peak is shown to increase linearly with the valence hole charge.

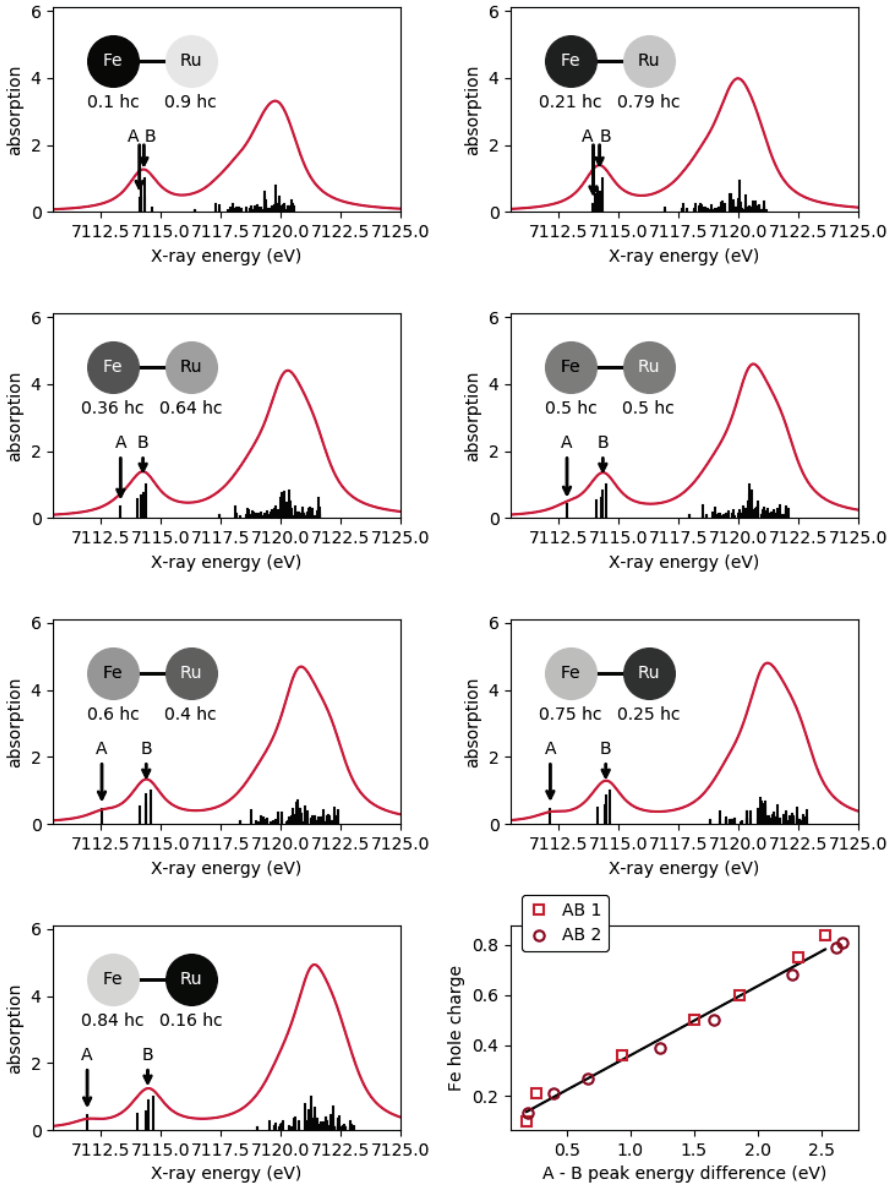

Figure S10: Computed spectrum with valence hole charge. The computed spectrum is shown for varying valence hole charge.

4.4 Molecular orbitals plots

Several different molecular orbitals contribute to the A, B, and C peaks, and we display these molecular orbitals here. We see that the A peak involves an orbital that is local to both the Fe and Ru atom, as well as the cyanide bridge. The B peak has contributions from orbitals that are much more delocalized throughout the molecule compared to the A peak. These orbitals have contributions into the solvent as well. The C peak involves molecular orbitals are delocalized from the molecule and involve the solvent.

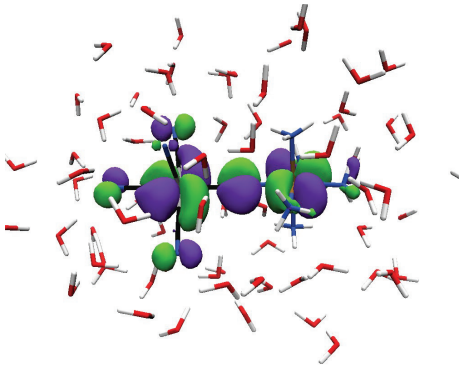

Figure S11: A peak molecular orbitals. Molecular orbital associated with the A peak, calculated at an Fe valence hole charge of 0.68. This orbital has an 86% contribution.

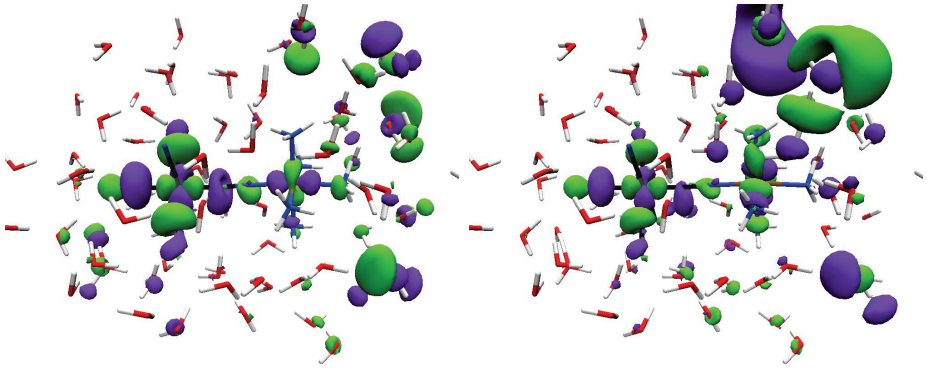

(a) This orbital has a 20% contribution (b) This orbital has a 9% contribution.

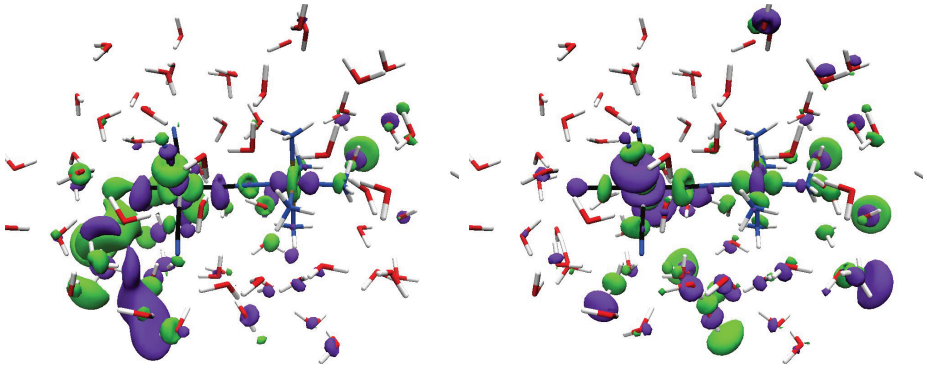

(c) This orbital has a 16% contribution (d) This orbital has a 15% contribution.

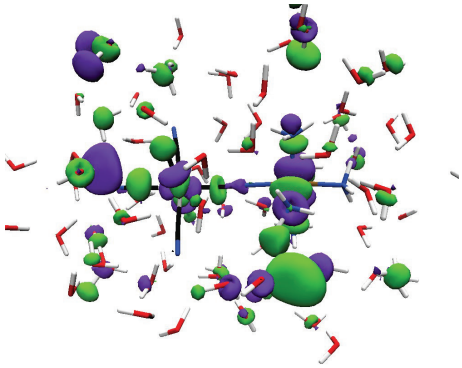

(e) This orbital has a 9% contribution.

Figure S12: B peak molecular orbitals. Molecular orbitals associated with the B peak, calculated at an Fe valence hole charge of 0.68.

References

1. Courtney, T. L.; Fox, Z. W.; Estergreen, L.; Khalil, M. Measuring Coherently Coupled Intramolecular Vibrational and Charge-Transfer Dynamics with Two-Dimensional Vibrational–Electronic Spectroscopy. *J. Phys. Chem. Lett.J. Phys. Chem. Lett.* **2015,** *6* (7), 1286-1292.
2. Slenkamp, K. M.; Lynch, M. S.; Van Kuiken, B. E.; Brookes, J. F.; Bannan, C. C.; Daifuku, S. L.; Khalil, M. Investigating vibrational anharmonic couplings in cyanide-bridged transition metal mixed valence complexes using two-dimensional infrared spectroscopy. *J. Chem. Phys.* **2014,** *140* (8), 084505.
3. Ross, M.; Andersen, A.; Fox, Z. W.; Zhang, Y.; Hong, K.; Lee, J.-H.; Cordones, A.; March, A. M.; Doumy, G.; Southworth, S. H.; Marcus, M. A.; Schoenlein, R. W.; Mukamel, S.; Govind, N.; Khalil, M. Comprehensive Experimental and Computational Spectroscopic Study of Hexacyanoferrate Complexes in Water: From Infrared to X-ray Wavelengths. *J. Phys. Chem. B* **2018,** *122* (19), 5075-5086.

4. James, G.; Witten, D.; Hastie, T.; Tibshirani, R. *An Introduction to Statistical Learning*. Springer New York: New York, NY, 2013; Vol. 103.
5. Aprà, E.; Bylaska, E. J.; Jong, W. A. d.; Govind, N.; Kowalski, K.; Straatsma, T. P.; Valiev, M.; Dam, H. J. J. v.; Alexeev, Y.; Anchell, J.; Anisimov, V.; Aquino, F. W.; Atta-Fynn, R.; Autschbach, J.; Bauman, N. P.; Becca, J. C.; Bernholdt, D. E.; Bhaskaran-Nair, K.; Bogatko, S.; Borowski, P.; Boschen, J.; Brabec, J.; Bruner, A.; Cauët, E.; Chen, Y.; Chuev, G. N.; Cramer, C. J.; Daily, J.; Deegan, M. J. O.; DunningJr., T. H.; Dupuis, M.; Dyall, K. G.; Fann, G. I.; Fischer, S. A.; Fonari, A.; Früchtl, H.; Gagliardi, L.; Garza, J.; Gawande, N.; Ghosh, S.; Glaesemann, K.; Götz, A. W.; Hammond, J.; Helms, V.; Hermes, E. D.; Hirao, K.; Hirata, S.; Jacquelin, M.; Jensen, L.; Johnson, B. G.; Jónsson, H.; Kendall, R. A.; Klemm, M.; Kobayashi, R.; Konkov, V.; Krishnamoorthy, S.; Krishnan, M.; Lin, Z.; Lins, R. D.; Littlefield, R. J.; Logsdail, A. J.; Lopata, K.; Ma, W.; Marenich, A. V.; Campo, J. M. d.; Mejia-Rodriguez, D.; Moore, J. E.; Mullin, J. M.; Nakajima, T.; Nascimento, D. R.; Nichols, J. A.; Nichols, P. J.; Nieplocha, J.; Otero-de-la-Roza, A.; Palmer, B.; Panyala, A.; Pirojsirikul, T.; Peng, B.; Peverati, R.; Pittner, J.; Pollack, L.; Richard, R. M.; Sadayappan, P.; Schatz, G. C.; Shelton, W. A.; Silverstein, D. W.; Smith, D. M. A.; Soares, T. A.; Song, D.; Swart, M.; Taylor, H. L.; Thomas, G. S.; Tipparaju, V.; Truhlar, D. G.; Tsemekhman, K.; Voorhis, T. V.; Vázquez-Mayagoitia, Á.; Verma, P.; Villa, O.; Vishnu, A.; Vogiatzis, K. D.; Wang, D.; Weare, J. H.; Williamson, M. J.; Windus, T. L.; Woliński, K.; Wong, A. T.; Wu, Q.; Yang, C.; Yu, Q.; Zacharias, M.; Zhang, Z.; Zhao, Y.; Harrison, R. J. NWChem: Past, present, and future. *J. Chem. Phys.* **2020,** *152* (18), 184102.
6. Valiev, M.; Bylaska, E. J.; Govind, N.; Kowalski, K.; Straatsma, T. P.; Van Dam, H. J. J.; Wang, D.; Nieplocha, J.; Apra, E.; Windus, T. L.; de Jong, W. NWChem: A comprehensive and scalable open-source solution for large scale molecular simulations. *Computer Physics Communications* **2010,** *181* (9), 1477-1489.

7. Biasin, E.; Fox, Z. W.; Andersen, A.; Ledbetter, K.; Kjær, K. S.; Alonso-Mori, R.; Carlstad, J. M.; Chollet, M.; Gaynor, J. D.; Glownia, J. M.; Hong, K.; Kroll, T.; Lee, J. H.; Liekhus-Schmaltz, C.; Reinhard, M.; Sokaras, D.; Zhang, Y.; Doumy, G.; March, A. M.; Southworth, S. H.; Mukamel, S.; Gaffney, K. J.; Schoenlein, R. W.; Govind, N.; Cordones, A. A.; Khalil, M. Direct observation of coherent femtosecond solvent reorganization coupled to intramolecular electron transfer. *Nature Chemistry* **2021,** *13* (4), 343-349.
8. Van Kuiken, B. E.; Valiev, M.; Daifuku, S. L.; Bannan, C.; Strader, M. L.; Cho, H.; Huse, N.; Schoenlein, R. W.; Govind, N.; Khalil, M. Simulating Ru L3-Edge X-ray Absorption Spectroscopy with Time-Dependent Density Functional Theory: Model Complexes and Electron Localization in Mixed-Valence Metal Dimers. *J. Phys. Chem. A* **2013,** *117* (21), 4444-4454.
9. Berendsen, H. J. C.; Grigera, J. R.; Straatsma, T. P. The missing term in effective pair potentials. *J. Phys. Chem.* **1987,** *91* (24), 6269-6271.
10. Joung, I. S.; Cheatham, T. E. Determination of Alkali and Halide Monovalent Ion Parameters for Use in Explicitly Solvated Biomolecular Simulations. *J. Phys. Chem. B* **2008,** *112* (30), 9020-9041.
11. Wang, J.; Wolf, R. M.; Caldwell, J. W.; Kollman, P. A.; Case, D. A. Development and testing of a general amber force field. *J. Comput. Chem.* **2004,** *25* (9), 1157-1174.
12. Cygan, R. T.; Liang, J.-J.; Kalinichev, A. G. Molecular Models of Hydroxide, Oxyhydroxide, and Clay Phases and the Development of a General Force Field. *J. Phys. Chem. B* **2004,** *108* (4), 1255-1266.
13. Adamo, C.; Barone, V. Toward reliable density functional methods without adjustable parameters: the PBE0 model. *J. Chem. Phys.* **1999,** *110* (13), 6158-6170.
14. Perdew, J. P.; Ernzerhof, M.; Burke, K. Rationale for mixing exact exchange with density functional approximations. *J. Chem. Phys.* **1996,** *105* (22), 9982-9985.

15. Krishnan, R.; Binkley, J. S.; Seeger, R.; Pople, J. A. Self-consistent Molecular Orbital Methods. XX. A Basis Set for Correlated Wave Functions. *J. Chem. Phys.* **1980,** *72*, 650-654.

16. Andrae, D.; Häußermann, U.; Dolg, M.; Stoll, H.; Preuß, H. Energy-adjustedab initio pseudopotentials for the second and third row transition elements. *Theor. Chim. Acta* **1990,** *77* (2), 123-141.

17. Dolg, M.; Wedig, U.; Stoll, H.; Preuss, H. Energy-adjusted ab initio pseudopotentials for the first row transition elements. *J. Chem. Phys.* **1987,** *86* (2), 866-872.

18. Ryckaert, J.-P.; Ciccotti, G.; Berendsen, H. J. C. Numerical integration of the cartesian equations of motion of a system with constraints: molecular dynamics of n-alkanes. *J. Comput. Phys.* **1977,** *23* (3), 327-341.

19. Berendsen, H. J. C.; Postma, J. P. M.; van Gunsteren, W. F.; DiNola, A.; Haak, J. R. Molecular dynamics with coupling to an external bath. *J. Chem. Phys.* **1984,** *81* (8), 3684-3690.

20. Silverstein, D. W.; Govind, N.; van Dam, H. J. J.; Jensen, L. Simulating One-Photon Absorption and Resonance Raman Scattering Spectra Using Analytical Excited State Energy Gradients within Time-Dependent Density Functional Theory. *J. Chem. Theory Comput.* **2013,** *9* (12), 5490-5503.

21. Lopata, K.; Van Kuiken, B. E.; Khalil, M.; Govind, N. Linear-Response and Real-Time Time-Dependent Density Functional Theory Studies of Core-Level Near-Edge X-Ray Absorption. *J. Chem. Theory Comput.* **2012,** *8* (9), 3284-3292.

22. Noro, T.; Sekiya, M.; Koga, T. Segmented contracted basis sets for atoms H through Xe: Sapporo-(DK)-nZP sets (n = D, T, Q). *Theor. Chem. Acc.* **2012,** *131* (2), 1124.